Structural Characterization of M^+CH_2 Products Formed by Reaction of 5d Metal Cations Pt^+ and Ir^+ with Ethylene Oxide and Ta^+ with Methane using Messenger Spectroscopy

Joost M. Bakker,*,§ Cameron J. Owen,† Sjoerd W. Nooteboom,§ Olga V. Lushchikova,§ and P. B. Armentrout†

§*Radboud University, Institute for Molecules and Materials, FELIX Laboratory, Toernooiveld 7, 6525 ED Nijmegen, The Netherlands*

†*Department of Chemistry, University of Utah, 315 S. 1400 E. Room 2020, Salt Lake City, Utah 84112, United States*

Abstract: Structural characterization of gas-phase $[M,C,2H]^+$ (M = Ta, Ir, Pt), formed by reacting laser ablation formed M^+ with ethylene oxide (c-C_2H_4O) or methane under multiple collision conditions, is achieved using infrared multiple photon dissociation (IR-MPD) spectroscopy with the intracavity free-electron laser FELICE. After product formation, part of the product distribution is complexed with Ar, allowing for simultaneous recording of IR-MPD spectra of both bare $[M,C,2H]^+$, which dissociates via dehydrogenation, and $[M,C,2H]^+\cdot Ar$, which loses Ar. Comparison of the spectra with density functional theory (DFT) calculations allows for an internally consistent assignment of the spectra to the Ta^+CH_2 ($^3A''$) distorted carbene, Pt^+CH_2 ($^2A_1$) carbene, and to the HIr^+CH ($^1A'$) carbyne-hydride. Evidence for a symmetric $Ta^+CH_2\cdot Ar$ ($^3B_2$) complex is also obtained. For Pt and Ir, these structures match those found in previous work when these species were formed by reaction of M^+ with methane, CH_4 and CD_4. Under the current conditions, no clear signs of the previously observed Ir^+CH_2 ($^3A_2$) carbene product were found, consistent with its higher energy, especially after Ar complexation. Potential energy surfaces for the reactions of Pt^+ and Ir^+ with c-C_2H_4O are also computed.

Keywords: action spectroscopy; CH bond activation; infrared multiple photon dissociation; potential energy surfaces

1. Introduction

Interactions between methane and transition metal cations have attracted wide interest because they can provide insight for the rational design of future methane activation catalysts.[1,2] As the most basic of reactions involving methane and metals, they also form benchmark systems for the development of theoretical methods describing the interactions with open-shell systems. Cations of five of the 3rd row transition metal elements (Ta, W, Os, Ir, and Pt) have been shown to dehydrogenate methane to form $[M,C,2H]^+$ ions at room temperature.[3–12] $[M,C,2H]^+$ can also be formed for additional metal cations at room temperature when they are reacted with either cyclopropane, c-C_3H_6, or ethylene oxide, c-C_2H_4O.[13–16] Understanding the structure of the $[M,C,2H]^+$ ions and the energetics of processes in which they are formed, including the trends observed along the periodic table, can provide deep understanding of the organometallic chemistry involved.[17]

In a recent series of publications, we have used infrared multiple-photon dissociation (IR-MPD) action spectroscopy to determine the structures of the dehydrogenation products $[M,C,2H]^+$. For M = Ta, W, Pt, and Au, the products adopt an M^+CH_2 carbene structure, which for M = Ta and W is distorted from C_{2v} symmetry by agostic interactions.[18–20] For M = Os and Ir, the structure is that of a carbyne-hydride, HM^+CH,[18–20] although Ir^+ also yielded smaller amounts of a second, higher-energy carbene isomer.

What simultaneously complicated *and* facilitated our spectroscopic studies is the fact that, at the finite temperatures at which the experiments were conducted, the vibrational bands are strongly broadened by rotational substructure associated with the relatively large rotational constants. Whereas the *a*-type transitions of asymmetric top molecules are still relatively condensed and simple to interpret, *b*- and *c*-type transitions exhibit a complex shape that, at room temperature, can lead to bands that easily extend over tens to hundreds of cm^{-1}. This rotational substructure can assist in identification of the vibrational transition. However, to profit from this enhancement, a spectroscopically sensitive scheme is required. Such schemes exist, for instance in the experiments devised by Schlemmer and co-workers, where reaction products are stored in ion traps at low-temperatures with a helium buffer gas, and the resonant absorption of IR photons hinders He complex formation, or leads to dissociation of He complexes formed.[21,22] In contrast, for IR-MPD to detect resonances, sequential absorption of several photons is required such that the total energy absorbed exceeds the fragmentation energy by an amount that dissociation occurs within the experimental time frame. This requirement demands a rapid dissipation of the absorbed photon's energy into the bath of vibrational degrees of freedom through intramolecular vibrational redistribution, a process known to be statistical and thus limited by the number of vibrational states available.[23,24] As a consequence, IR-MPD spectroscopy of these stable and small (four atom) cations has not been easy: irradiation of $[M,C,2H]^+$ (M = Ta, Ir, and Pt) using the light produced by the infrared free-electron laser FELIX did *not* result in observed fragmentation.[25–27] It took the pulse energies of the intracavity free-electron laser FELICE to succeed in resonant fragmentation,[16,18–20] but the intensities required to overcome the fragmentation energy also led to broadening effects, prohibiting the observation of individual ro-vibrational transitions.

In analogy to Schlemmer's methods, vibrational spectra of $[M,C,2H]^+$ ions can also be recorded using the messenger spectroscopy method.[28] Here, the ion of interest is complexed with a weakly bound species, often a rare gas atom, which is eliminated from the complex upon IR excitation. The binding energy of the messenger is typically substantially lower than what is required to break covalent bonds in the ion of interest, and because the vibrational density of states (DOS) increases with the number of constituent atoms, both IRMPD conditions are simultaneously relaxed. The essence of messenger spectroscopy is that it should not change the nature of the ion under investigation, but complexation with a messenger atom will result in a change of the moments of inertia, and therefore in a change in the rotational constants. If this is the case, one can foresee that the rotational structure of a band may collapse, yielding significantly narrower bands.

In this work, we present IR-MPD spectra of three $[M,C,2H]^+{\cdot}Ar$ (M = Ta, Pt, Ir) complexes along with $[Ir,C,2H]^+ Ar_2$. The work was carried out using IR light generated by the FELICE instrument in the same experimental apparatus as used in the previous publications.[16,18–20] As the complexation of $[M,C,2H]^+$ is not 100% efficient, and the intensity of the intracavity laser is sufficient to induce dehydrogenation of the bare systems, we will be able to compare the two spectra. Two of the systems under study $[M,C,2H]^+$ (M = Pt and Ir) were prepared by reacting the atomic metal cations with ethylene oxide (oxirane), c-C_2H_4O, allowing us to verify whether the structures of the $[M,C,2H]^+$ products are the same as the ones produced using methane.

2. Experimental and Computational Methods

2.1. Experiment

Key parts of the experimental apparatus are shown in Figure S1. M^+ ions were produced by ablating a rod of the precursor metal (solid Ta, or a 0.1 mm thick Pt or Ir foil spot welded onto a stainless steel rod) with the second harmonic of a pulsed Nd:YAG laser (532 nm) in the presence of 10 % argon admixed with helium, which cooled and entrained the generated ions down a 3 mm diameter, 60 mm long channel. The channel was segmented into two parts: a room temperature stainless steel part where the ablation took place (35 mm long from the point of ablation), and a copper part (45 mm long) that can be temperature controlled by liquid nitrogen and resistive heaters. The two parts were separated by a 4 mm thick PEEK disk to thermally isolate the copper part. Approximately 64 mm downstream from the ablation source, the ions were exposed to a pulse of 5% ethylene oxide or methane diluted in helium. Pulses of the Ar/He carrier gas and the reactant gases were adjusted such that minor amounts of products from the M^+ + c-C_2H_4O/CH_4 reactions were formed. The temperature of the second part of the channel was kept at 243 K to facilitate complexation of product ions with Ar atoms. After the initial reaction, the gas mixture was expanded into vacuum forming a molecular beam. The beam then passed through a 2 mm diameter conical skimmer and a 0.45 mm slit aperture (both electrically grounded) before entering the source region of a reflectron time-of-flight mass spectrometer (Jordan TOF Products, Inc). Here, the ions formed were irradiated by IR laser light, and then a few microseconds after irradiation, all ions were pulse-extracted into the mass spectrometer, mass analyzed, and detected with microchannel plates. To enhance the ability to observe depletion of the $[M,C,2H]^+\cdot Ar$ species, a movable slit aperture was positioned in the path of the mass-spectrometer.[29]

The experiment is coupled to the Free-Electron Laser for IntraCavity Experiments (FELICE) at the Free Electron Lasers for Infrared eXperiments (FELIX) Laboratory in the Netherlands.[30] The molecular beam crosses the laser beam at a 35° angle and can be translated with respect to laser beam height and focal point, as previously described.[30] The laser macropulse was typically 8 μs in duration and consisted of picosecond-long near-transform limited micropulses at a 1 ns separation. In the current work, the experiment was positioned as far from the focus as possible. Pulse energies inferred from a fraction of outcoupled light were typically in the 0.5 – 2 J range. The out-of-focus position then translates to a maximum fluence of 16 J/cm^{-2} at 1400 cm^{-1}. The spectral width was set to approximately 0.6% full-width at half-maximum (FWHM) of the central frequency. By operating the experiment at twice the IR laser repetition rate, two sets of mass spectra were generated in alternating fashion, yielding mass intensities $I_{sig}(v)$ with IR exposure at frequency v, and I_{ref} without IR exposure. IR-MPD spectra were recorded by varying the IR frequency with steps of 2.5 cm^{-1}.

Two methods were used to further treat the experimental data: depletion and growth spectroscopy. Depletion of the mass intensity of the ion of interest results from its fragmentation after having absorbed IR energy in excess of the decomposition barriers. The formula used to calculate the depletion yield was the logarithmic ratio of the ion intensity without and with irradition, $\ln(I_{ref}/I_{sig}(v))$. Depletion spectra clearly stem from the mass in question, but are not background-free, and thus inherently noisy. If the ion of interest fragments upon irradiation, and the fragment ion mass channel is empty before irradiation, a better signal-to-noise spectrum can be determined through the fragmentation yield, calculated as $\ln(1+ I_{sig,F}/I_{sig,P})$, where P and F represent the precursor and fragment ions. Because the $[M,C,2H]^+$ mass channel was not empty prior to irradiation, *vide infra*, the Ar-tagged complexes were evaluated using depletion spectroscopy, while spectra for the bare $[M,C,2H]^+$ species were constructed via growth spectroscopy using either the $[M,C]^+$ or $[M,C,H]^+$ fragment. For both types of spectra, the yields calculated as above were corrected for variation of the IR pulse energy.

2.2 Quantum Chemical Calculations

To interpret the observed spectra and evaluate binding energies, density functional theory (DFT) calculations were performed. Geometries were optimized with the B3LYP hybrid functional and the def2-TZVPPD basis set, referred to in this work as "def2". The def2 basis set is a balanced triple-ζ valence basis set with double polarization and a diffuse function on all elements. For C, H, and Ar atoms, def2 is an all-electron basis set, whereas for the metal elements, it has a small-core (46 electron) effective core potential (ECP), while the 5s, 5p, 6s, 6p, and 5d electrons are treated explicitly. This approach was successfully used in our previous IR-MPD spectroscopic studies of products formed in the reactions of 5d transition metal cations with methane and multiple methane reactant gases.[16,18–20,25–27] To include dispersive interactions, Grimme's D3 dispersion correction scheme was employed.[31]

To facilitate comparisons between experimental spectra and the theoretically predicted vibrational frequencies and IR intensities, each calculated frequency was scaled by a uniform scaling factor, used to specifically account for anharmonicity, red-shifting, and other deficiencies within the theoretical spectra associated with the absorption of multiple photons in the IR-MPD process. Scaling factors used were 0.939 or 0.95 for spectra inferred from dehydrogenation (as determined in previous work),[19] whereas a factor of 0.975 was used for spectra based on Ar-loss. The broadening resulting from rotational substructure of each band was taken into account by calculating the rotational transition frequencies and intensities for pure *a*-, *b*-, and *c*-type transitions. Table S1 lists the rotational constants for all species. For each vibrational transition, classified as *a*-, *b*-, or *c*-type, the resulting rotation-vibrational transition structure was simulated by weighting each rotational transition with the thermal (77 or 293 K) population of the originating rotational level in the ground vibrational state, and by the calculated IR intensity of the vibrational band. The resulting transition structure was then shifted by the (scaled) harmonic frequency and convoluted with a Gaussian line shape function having a FWHM of 0.6% of the frequency, replicating the FELICE spectral bandwidth.

Potential energy surfaces for the reactions of Pt^+ and Ir^+ with ethylene oxide were also examined at the B3LYP/def2 level of theory. Transition states (TSs) were identified as having a single imaginary frequency and all intermediates as having none. Energies provided are corrected for zero-point energy contributions using unscaled frequencies. These calculations are designed primarily to show feasible pathways for the observed reactions and are not intended to be fully quantitative. For example, at this level of theory, the bond energy for forming CH_2 ($^3B_1$) + CH_2O from ethylene oxide is calculated to be 3.19 eV, somewhat lower than the experimental value of 3.376 eV.[32] However, these calculations overestimate the bond energies of Pt^+CH_2 ($^2A_1$) and HIr^+CH ($^1A'$), 5.08 and 5.52 eV, compared to experimental values of 4.80 ± 0.03 and 4.92 ± 0.03 eV, respectively.[6,9]

3. Results and discussion

3.1 Platinum - Spectroscopy

Upon reacting Pt^+ with ethylene oxide in the carrier gas mixture, several product masses are observed. The mass spectrum (Figure S2) recorded under typical experimental conditions is dominated by the bare Pt^+ ion having isotopes at 192 (0.8%), 194 (33.0%), 195 (33.8%), 196 (25.2%), and 198 (7.2%). The second most abundant mass channel is that for $[Pt,C,2H]^+$, with smaller contributions of $[Pt,2C,2H]^+$, $[Pt,2C,4H]^+$, and what may be $[Pt,C,O,H]^+$. No significant PtO^+ was observed, and a tiny signal was found at the mass corresponding to Pt^+ with an ethylene oxide adduct. Minor signals were further found at masses corresponding to the complexes of the previously mentioned products plus ethylene oxide. The presence of Ar in the carrier gas was revealed by $Pt^+\cdot Ar$ and $Pt^+\cdot Ar_2$ complexes, as well as by the $[Pt,C,2H]^+\cdot Ar$ product. Further minor mass channels were formed by what is likely a complex of $[Pt,C,O,H]^+$ with Ar, and of $[Pt,C,2H]^+$ with both ethylene oxide and Ar.

In our previous work investigating the structure of $[Pt,C,2H]^+$ formed by reacting Pt^+ with methane, we observed a spectrum by monitoring the loss of H from $[Pt,C,2H]^+$.[19] Because the complexation of the ion with Ar is not 100%, we still observe the bare $[Pt,C,2H]^+$ ion with appreciable intensity. With the fluences in our current experiment still sufficient to fragment

$[Pt,C,2H]^+$, we could simultaneously record a spectrum of the bare ion by monitoring appearance of $[Pt,C,H]^+$. This growth spectrum is depicted in the top panel of Figure 1a by the black trace. It exhibits only two bands, one at 746 cm^{-1} and one at 991 cm^{-1}. In the same panel, the spectrum recorded earlier is shown as the red curve.[19] The current spectrum differs from that recorded previously in several ways. First, the former spectrum exhibited a band at 665 cm^{-1} (one could argue that the current spectrum exhibits a tail from the 746 cm^{-1} band towards these lower frequencies) and a weak band at about 1310 cm^{-1}. Second, the intensity ratio of the 746 and 991 cm^{-1} bands is significantly different. Third, the 991 cm^{-1} band appears to have shifted towards the blue in the present spectrum. We attribute this latter effect to a slight difference in the wavelength calibrations (which are ordinarily within 5 cm^{-1}), whereas the first difference is likely a result of the lower fluence conditions under which the current spectrum is recorded. In this context, the reader is reminded that IR-MPD is a technique that is linear with the laser fluence once a certain threshold has been overcome,[33–35] but this threshold is mode-dependent and larger for lower frequency modes where more photons are required for fragmentation.

When the $[Pt,C,2H]^+\cdot Ar$ was irradiated resonantly, the signal intensity observed in the m/z = 248-250 and 252 mass channel was reduced, and there was no sign of growth resulting from fragmentation of larger species. We thus conclude that the depletion spectrum of $[Pt,C,2H]^+\cdot Ar$ is clean and representative of this isolated mass. Its depletion spectrum is depicted in the top panel in Figure 1b. The spectrum is dominated by a broad structured band centered around 1050 cm^{-1}, with a second intense, but much narrower band at 752 cm^{-1}. The latter is accompanied by two distinct sharp bands at 674 and 708 cm^{-1}, respectively. A final, weaker band is discerned around 1360 cm^{-1}.

To interpret the experimental spectra, they are compared to two types of calculated spectra: stick spectra (blue bars), representing the harmonic frequencies and associated IR intensities calculated using the DFT methods described above, and the full rotational spectra (lines) simulated at a specified temperature. Below the experimental spectrum in Figure 1a, the calculated spectrum for the bare Pt^+CH_2 carbene, simulated at 77 K, shows reasonable agreement with the present experimental spectrum. Given that the calculated energy for H elimination from this molecule is 3.60 ± 0.11 eV,[6] it is no surprise that only the strongest bands are seen for fragmentation of the bare ion. Both harmonic frequencies and the simulated rovibrational spectra are scaled with the 0.939 factor used in our previous work.[19] For the 991 cm^{-1} band, the observed peak is narrower than expected on the basis of the predicted rotational contours at 77 K. This comparison suggests that the temperature may be lower, which would reduce the spacing between the two branches of this *c*-type band. This conjecture is consistent with the narrower band at 746 cm^{-1} compared to predictions as well.

The spectra simulated for the $[Pt,C,2H]^+ \cdot Ar$ complex have been scaled by a factor 0.975 to compensate for anharmonicities, and appear to describe the experimental spectrum quite accurately, Figure 1b. They are calculated for a $Pt^+CH_2 \cdot Ar$ ($^2A_1$) carbene structure, where the Ar is bound to the Pt such that C-Pt-Ar is linear, keeping the Pt^+CH_2 C_{2v} symmetry intact. In this case two curves are shown, simulated at temperatures of 77 K (black curve) and 293 K (red). The binding energy of the Ar was calculated to be 0.43 eV, implying that at 752 cm^{-1} at least five photons must be absorbed to eliminate the Ar. This weak bond is evidenced by an observed depletion of the Ar-tagged species down to ~10% for the strongest bands. The intense, narrow band at 752 cm^{-1} is readily assigned to the intense Pt-C stretching mode, calculated at 735 cm^{-1}. As the transition dipole for this vibrational mode is along the main axis of inertia, this is an *a*-type transition where all substructure collapses into one band upon convoluting the individual rotational levels with a Gaussian lineshape function representing the laser spectral width. On the other hand, the broad 1050 cm^{-1} band is the CH_2 out-of-plane bending mode (calculated frequency 1031 cm^{-1}), which is a *c*-type transition. Although the integrated IR intensity of this band is larger, as seen in the stick spectrum, the intensity is diluted over a much broader band and clearly exhibits substructure. For this band, the comparison between spectra calculated for 77 K and 293 K appears to favor the lower temperature, as it predicts the 1050 cm^{-1} band somewhat better (both in terms of the relative intensities of the main peaks and side bands and the overall width of the band). Failure to observe the clear double-peaked structure as predicted in the simulation leads us to speculate that this band is saturated. This hypothesis is also consistent with the mismatch in relative intensities for the two experimental bands at 674 and 708 cm^{-1} with respect to that of the main band at 752 cm^{-1}, in comparison to the simulated spectra. The potential band at 1360 cm^{-1} could be assigned to the 1387 cm^{-1} *a*-type in-plane CH_2 scissoring mode. Regarding the two bands at 674 and 708 cm^{-1}, the only calculated band with appreciable IR intensity in this region is the in-plane CH_2 bending mode. This mode is calculated at 720 cm^{-1}, falling close to the strong band at 735 cm^{-1}. If this band is shifted down by 40 cm^{-1} (as shown in Figure 1b), the double-peak structure characteristic for this *b*-type transition, now matches the experimental band structure quite well. We have applied the same 40 cm^{-1} down shift to the in-plane CH_2 bending mode in the simulated spectrum for bare Pt^+CH_2, Figure 1a. There we see quite reasonable agreement with the observed bands in both the previous and present spectra, perhaps even recognizing the predicted substructure in the present spectrum. All observed band frequencies for $[Pt,C,2H]^+$ and $[Pt,C,2H]^+\cdot Ar$, together with their assigned calculated normal mode frequencies and a mode description are listed in Table 1, which also includes values for the M = Ir and Ta systems discussed below.

If we compare the calculated spectra for the bare Pt^+CH_2 with that of its Ar-complex, we note that the addition of Ar leads to significant changes in the spectrum, but a drastic reduction in observed line widths is not found. The rovibrational simulation for the Ar complex is slightly sharper, mainly reflecting the change in the B and C rotational constants (A = 9.6687, B = 0.0553, and C = 0.0550 cm^{-1} for the Ar complex versus A = 9.4815, B = 0.3537, and C = 0.3410 cm^{-1} for the bare ion). Thus, because the Ar is attached on the symmetry axis, thereby not breaking C_{2v} symmetry, its addition does not allow for much higher resolution through the collapse of the rotational profile. Although not directly relevant here, it is of interest to note that the tagging atom's influence on the rotational constants may be underestimated in DFT calculations because of zero-point motion.[36] On the other hand, the lower binding energy of the Ar does allow the use of lower IR intensity, revealing the minor band at 1360 cm^{-1} as well as substructure in the 680 and 1050 cm^{-1} bands not discernible in spectra monitoring the direct fragmentation of the Pt^+CH_2 carbene.

3.2 Platinum – Reaction Mechanism

The formation of the platinum carbene from the reaction of atomic platinum cations with ethylene oxide is straightforward and shown in Figure 2. All species have doublet spin (except for the ethylene oxide reactant and formaldehyde product). Initially, the reaction forms a Pt^+(c-C_2H_4O) adduct, intermediate **1**. Activation of one of the CO bonds through **TS1/2** leads to the cyclic intermediate **2**, c-$PtOCH_2CH_2^+$. Cleavage of the CC bond through **TS2/3** gives a formaldehyde adduct of $PtCH_2^+$, intermediate **3**, which can easily lose the CH_2O ligand to form the final $PtCH_2^+$ product. The overall reaction is calculated to be exothermic by 1.89 eV and all intermediates and transition states lie at least 1.5 eV below the reactants. Clearly, the Ar adduct can be formed during the collisional cooling of these products.

3.3 Iridium - Spectroscopy

The product distribution formed upon reacting Ir^+ with c-C_2H_4O shows a similar pattern as that for Pt^+ (Figure S3), with the atomic ion being dominant and showing both the 191 (37.3%) and 193 (62.7%) isotopes. $[Ir,C,2H]^+$, $[Ir,2C,2H]^+$, and $[Ir,2C,4H]^+$ product ions are most abundant. In contrast to the reaction with Pt^+, an $[Ir,2C,O,2H]^+$ product, presumably resulting from single dehydrogenation of c-C_2H_4O, is also found with an intensity comparable to that for $[Ir,C,2H]^+$. The $[Ir,C,2H]^+$ product is found with one and two Ar adducts, and with a mass coinciding with a c-C_2H_4O adduct as well.

Just as for the spectrum of bare $[Pt,C,2H]^+$, that for $[Ir,C,2H]^+$ (Figure 3a, black trace), obtained as the growth spectrum for $^{191}IrC^+$, shows fewer bands than the one published previously,[19] shown in red in Figure 3a. The current spectrum shows a triad of close-lying bands at 663, 701, and 751 cm^{-1}, respectively, and a broad 'bump' around 875 cm^{-1}. This 'bump' and the sharp 751 cm^{-1} band appear in contrast with the spectrum in red. The $[Ir,C,2H]^+$ products formed by reacting Ir^+ with methane were previously identified as a combination of a HIr^+CH ($^1A'$) carbyne-hydride and smaller amounts of a Ir^+CH_2 ($^3A_2$) carbene, both formed exothermically with respect to the Ir^+ + CH_4 reactants. In the previous work, bands at 656, 694, 1034 (as well as 2198 and 2940) cm^{-1} were assigned to the carbyne-hydride, and those at 961 and 1301 (as well as 1933) cm^{-1} corresponded to the carbene.

When simulating the rotational structure of the spectrum of the carbyne-hydride, we previously found that shifting the C-H out-of-plane bending mode (calculated at 747 cm^{-1}) by 60 cm^{-1} provided a much improved match with experiment.[20] If we also do this here and compare to the current IR spectrum, Figure 3b, the 77 K simulated band of HIr^{+}CH, although slightly broader, favorably compares to the left two bands of the triad, and to the spectrum in red (where the high-frequency tail was assigned to the Ir-C stretch mode of the carbene at 733 cm^{-1}), but cannot explain the rightmost band at 751 cm^{-1} nor the 'bump'. The 751 cm^{-1} band could be assigned to the Ir-C stretch mode of the carbene, Figure 3c, but that species is predicted to have a stronger band at 972 cm^{-1} (the CH$_2$ out-of-plane bend) that was observed in the red spectrum, but is not apparent under the current conditions.

Neither the carbyne-hydride nor the carbene can explain the 875 cm^{-1} 'bump', and neither this nor the 751 cm^{-1} band are consistent with the previous spectrum for [Ir,C,2H]$^{+}$ formed when reacting Ir^{+} with methane.[19] Thus, we considered whether there was another source for these bands. For this, we consider the [Ir,2C,O,2H]$^{+}$ product, presumably resulting from single dehydrogenation of c-C$_2$H$_4$O. Upon IR irradiation, this species shows resonance depletion bands (recorded by growth of ^{191}IrC^{+}, Figure 3d) that coincide with the rightmost triad band and the bump observed in the [Ir,C,2H]$^{+}$ spectrum. Inspection of the mass spectra for possible photofragmentation products indicates that the appearance of ^{191}IrC^{+} (loss of [C,O,2H] from [Ir,2C,O,2H]$^{+}$) forms a high-energy loss channel (only visible at the peak of the 751 cm^{-1} depletion and not intense enough to explain the full intensity loss observed). A loss of CO would leave the mass of the [Ir,C,2H]$^{+}$ product, for which the growth (recorded in the [^{193}Ir,C,2H]$^{+}$ channel) mirrors the depletion of [Ir,2C,O,2H]$^{+}$, as evident in Figure 3d. A [Ir,C,2H]$^{+}$ species formed from photofragmentation is likely to retain internal energy that is not easily dissipated, such that it could either directly fragment further or could non-resonantly absorb further photons to eliminate H$_2$ and appear in the growth spectrum recorded in the ^{191}IrC^{+} mass channel, Figure 3a. Figure 3e shows the calculated spectrum for $OIrCHCH^+$ ($^3A'$), which clearly matches the depletion spectrum of $[Ir,C,O,2H]^+$ in Figure 3d well.

The IR spectrum for the $[Ir,C,2H]^+$ ion complexed with a single Ar (the depletion spectrum of $[Ir,C,2H]^+{\cdot}Ar$) is shown in Figure 4a. It is dominated by two bands centered at 673 and 756 cm^{-1} with widths of approximately 60 cm^{-1} FWHM. A third band can be discerned at 1059 cm^{-1}. Although the signal-to-noise ratio of the spectrum is modest, and the noise is notably larger towards the 1500 cm^{-1} spectrum edge (amplified by the pulse energy correction), it is possible that a fourth band around 1360 cm^{-1} can be discerned. The $[Ir,C,2H]^+$ products formed by reacting Ir^+ with methane were previously identified as a combination of a HIr^+CH ($^1A'$) carbyne-hydride and smaller amounts of a Ir^+CH_2 ($^3A_2$) carbene, with the former calculated to lie 0.25 eV below the latter.[19] At the current level of theory, we find the same values. The binding of Ar to the carbyne-hydride (0.47 eV) is significantly stronger than to the carbene (0.36 eV), such that the carbyne-hydride-Ar complex now lies 0.36 eV below the carbene-Ar complex. Thus, it can be expected that the IR spectrum for $[Ir,C,2H]^+{\cdot}Ar$ is biased towards the carbyne-hydride. Indeed, the two main bands can be identified as the concerted in-plane bending of the H-C-Ir-H group at 657 cm^{-1} and the C-H out-of-plane bending mode predicted at 806 cm^{-1} but shown in Figure 4a shifted to 748 cm^{-1}. The broadening of both bands is a result of the *b*- and *c*-type character of the transitions. The red trace in Figure 4a depicts a simulation of the spectrum at 293 K, giving a substantial broadening and overlap of the two bands. Thus, we again conclude that the estimate of 77 K (black trace) better reflects the temperature of the beam. The band at 1059 cm^{-1} can be identified as the Ir-C stretch mode in the carbyne-hydride (calculated 1084 cm^{-1}), which has a narrow rotational envelope characteristic of *a*-type transitions. It is difficult to assess whether the preferred Ar binding to the carbyne-hydride results in any appreciable formation of the carbene, as there is little sign of the main band predicted at 1005 cm^{-1}. Another band at 738 cm^{-1} is also predicted, but this coincides with the carbyne-hydride band at 748 cm^{-1} (after being shifted down). Only the weak perceived band at 1360 cm^{-1} (calculated 1402 cm^{-1}, CH_2 in-plane bending) could be a sign of the carbene, if that band is truly there.

Complexation with Ar has allowed for confirmation of the formation of the previously assigned minimum energy carbyne-hydride HIr^+CH structure. Again, the addition of Ar has not achieved a significant reduction in the spectral widths of the bands observed, confirming that the Ar does not significantly change the principal moment of inertia, i.e., it must attach more or less along the Ir-C axis, as also suggested by calculations on this species, Figure 4a. Interestingly, this result is in contrast with the depletion spectrum of the $[Ir,C,2H]^+\cdot Ar_2$ ion complex. Its spectrum is shown in Figure 4b, and exhibits two significantly narrower bands at 708 and 782 cm^{-1} with a FWHM of less than 30 cm^{-1}, as well as a sharp band at 1088 cm^{-1}. The narrower bands indicate that the second Ar (or both Ar) binds to a location off the principal axis. It is compared to a spectrum calculated for two Ar attached to the carbyne-hydride HIr^+CH structure, where both Ar are bound to the Ir in the H-Ir-C-H plane. The resulting structure has C_s symmetry ($^1A'$ ground state) and exhibits two intense bands predicted at 688 and 747 cm^{-1} (scaled by 0.975, with the latter CH out-of-plane bending mode first shifted down by 60 cm^{-1}). The rotational envelope now directly reflects that the second Ar has been added off the Ir-C axis. This is evidenced by a significant reduction in the A constant, going from $HIr^+CH\cdot Ar$ to $HIr^+CH\cdot Ar_2$ (5.5026 to 0.0669 cm^{-1}). The reduction is most obvious for *b*- and *c*-type transitions, which can be seen by comparing the simulated spectrum to that for $HIr^+CH\cdot Ar$: the 688 and 747 cm^{-1} bands (*b*- and *c*-type) are significantly reduced in width, whereas the width of the *a*-type band at 1088 cm^{-1} has barely changed.

3.4 Iridium – Reaction Mechanism

The potential energy surfaces for formation of $[Ir,C,2H]^+$ products from reaction of atomic iridium cations with ethylene oxide are shown in Figure 5. The ground state Ir^+ (^5F) and low-lying ^3F excited state follow a mechanism directly analogous to that for Pt^+ (^2D). Only the triplet species are shown in Figure 5b, with the quintet species being very similar. Coupling to the singlet surface is required in order to form the HIr^+CH ($^1A'$) product observed experimentally. Along the singlet surface, after CO bond activation to form the cyclic c-$IrOCH_2CH_2^+$ intermediate ^{1}**2**, a hydrogen atom transfer over ^{1}**TS2/4** yields intermediate ^{1}**4**, c-$HIrOCH_2CH^+$. Cleavage of the CC bond over ^{1}**TS4/5** then yields the HIr^+CH species complexed to formaldehyde, intermediate ^{1}**5**, which can easily lose the ligand to yield the final products. Coupling between the high-spin surfaces and this singlet surface can presumably occur most readily in the vicinity of intermediates **1** and **2**.

Figure 6 shows the triplet-spin potential energy surface for the dehydrogenation reaction forming the $OIrCHCH^+$ species observed experimentally, Figure 3e. Starting from the cyclic intermediate ^{3}**2**, c-$IrOCH_2CH_2^+$, activation of the CO bond over ^{3}**TS2/6** yields the $OIrCH_2CH_2^+$ intermediate ^{3}**6**, which can then transfer a hydrogen to Ir to form $(Ht)OIrCHCH_2^+$, ^{3}**7**. Here, the hydrogen is oriented trans to the CH_2 group (as indicated by t). Rearrangement of the hydrogen ligand position over ^{3}**TS7/8** forms $(Hc)OIrCHCH_2^+$, ^{3}**8**, where the hydrogen is now in a cis orientation relative to CH_2. This conformation allows transfer of another hydrogen atom to the iridium center over ^{3}**TS8/9** to form the dihydride, $(H)_2OIrCHCH^+$, ^{3}**9**. Coupling of the two hydride ligands over ^{3}**TS9/10** forms the dihydrogen adduct of the final product, $(H_2)OIrCHCH^+$, ^{3}**10**. Overall, the dehydrogenation reaction is exothermic by 2.34 eV compared to the Ir^+ (^5F) + c-C_2H_4O reactants, with ^{3}**TS1/2** being the rate-limiting step (followed by ^{3}**TS8/9**). As shown in Figure 6a, the pathway to form $IrCH_2^+$ ($^3A_2$) + CH_2O requires slightly more energy than ^{3}**TS8/9**, suggesting a reason why this latter product is not observed. We also considered whether dehydrogenation might occur from the four-membered cyclic species, but this yields c-$IrOCHCH^+$, which has a high barrier for transformation to $OIrCHCH^+$. (This TS lies 1.02 eV below the Ir^+ (^5F) + c-C_2H_4O reactants, such that this process should not be competitive with that shown in Figure 6.)

Finally, we examined how the $OIrCHCH^+$ product can rearrange to expel CO and form HIr^+CH ($^1A'$). The potential energy surface shown in Figure 7 starts at the triplet-spin $OIrCHCH^+$ product, ^{3}**CO1**. Its singlet spin analogue lies 0.68 eV higher. Twisting of the C_2H_2 ligand allows access to ^{3}**TSCO1/2** leading to c-$IrOCHCH^+$, intermediate ^{3}**CO2**. An analogous transformation could not be located on the singlet surface. From ^{3}**CO2**, cleavage of the IrO bond over ^{3}**TSCO2/3** leads to $IrCHCHO^+$, ^{3}**CO3**, which can now transfer a hydrogen to the iridium center over ^{3}**TSCO3/4**. This yields the $HIrCHCO^+$ intermediate ^{3}**CO4**, from which CO can be lost and form

$HIrCH^+$ ($^3A'$) + CO. An analogous pathway between **¹CO2** and **¹CO4** was located along the singlet surface with intermediates and TSs that are very similar to those shown for the triplet surface (and hence are not included in Figure 7b). Conversion from the initial triplet surface to the singlet surface that yields the ground state $HIrCH^+$ ($^1A'$) + CO products can presumably occur at both **¹CO2** and **¹CO4**, as both intermediates have similar energies to the triplet analogues.

3.5 Tantalum - Spectroscopy

In the case of Ta^+, ethylene oxide could not be used because this reaction produces primarily TaO^+. Therefore, methane was used as the reactive precursor in the carrier gas mixture. Several product masses are observed as shown by the mass spectrum in Figure S4. The dominant species is the bare Ta^+ ion having its single isotope at 181 followed by the $[Ta,C,2H]^+$ product. Smaller amounts of Ta^+ and $[Ta,C,2H]^+$ adducts each with one methane, two methanes, one Ar, and one Ar + one methane are also observed. The only other species is $[Ta,2C,4H]^+$ and its adduct with one Ar + one methane.

As in our previous work investigating the structure of $[Ta,C,2H]^+$ formed by reacting Ta^+ with methane, we observed a spectrum by monitoring the loss of H from $[Ta,C,2H]^+$.[19] The growth spectrum of $[Ta,C,H]^+$ is depicted in the top panel of Figure 8a by the black trace and compared with the spectrum recorded earlier (red curve).[19] The agreement between the two spectra is clearly good although a shift is obvious for the two intense bands peaking at 700 and 846 cm^{-1} in the current spectrum. This is apparently a difference in wavelength calibrations similar to that noted above for the Pt system. Notably, the band at 700 cm^{-1} exhibits structure that is reproduced in the previous spectrum but slightly better defined. The spacing and relative intensities of this spectral structure are well reproduced by the 77 K rotationally resolved band shown in the lower panel of Figure 8a. (Here, both harmonic frequencies and the simulated rovibrational spectra are scaled with the 0.98 factor used in our previous work.[20]) As before, the observed spectrum can be attributed to the ground state $TaCH_2^+$ ($^3A''$), an agostically distorted carbene structure. (There could also be contributions from a $^3A'$ state, which has an identical spectrum and is calculated to lie only 0.032 eV higher in energy.[10,19] The 699 cm^{-1} predicted band is the out-of-plane wag of the hydrogen lying nearly along the principal axis and has a *c*-type transition, Table 1. The 850 cm^{-1} band is the Ta-C stretch and the 1304 cm^{-1} band is the CH_2 scissoring bend, both of which are *b*-type transitions.

When the $[Ta,C,2H]^+\cdot Ar$ ion was irradiated resonantly, the signal intensity observed in the *m/z* = 235 mass channel was reduced, and there was no sign of growth resulting from fragmentation of larger species. We thus conclude that the depletion spectrum of $[Ta,C,2H]^+\cdot Ar$ is clean and representative of this isolated mass. Its depletion spectrum is depicted in the top panel in Figure 8b. The spectrum is dominated by a broad structured band centered around 710 cm^{-1} that is narrower than the comparable band in the $[Ta,C,2H]^+$ spectrum, suggesting that the Ar must be bound off the principal axis. The band at 850 cm^{-1} in the bare ion spectrum is reproduced but now accompanied by a pair of bands at 910 and 940 cm^{-1}. Likewise, the broad band at 1334 cm^{-1} in the bare spectrum reappears for the Ar adduct, slightly blue-shifted and with more structure and accompanied by two additional bands at 1192 and 1244 cm^{-1}. Clearly, the adduct spectrum must represent several species.

Because of the asymmetry of the distorted $TaCH_2^+$ species, a number of low-lying Ar adducts could be located. When the Ar remains in the plane of the carbene, $^3A'$, $^3A''$, and $^1A'$ states could all be located and have similar spectra. Here, the ground state is $^3A''$ with the $^3A'$ and $^1A'$ states lying 0.005 and 0.417 eV higher in energy. Further, the Ar can attach perpendicular to the plane of the carbene, yielding a ^3A state, 0.016 eV above the $^3A''$ ground state. All four spectra contain the same three bands observed for the bare carbene, each with systematic shifts, but are narrower because of the much smaller rotational constant induced by the presence of the Ar. These spectra simulated for the $[Ta,C,2H]^+\cdot Ar$ complex have been scaled by a factor 0.975 to compensate for anharmonicities, but appear to describe the experimental bands observed at 700, 850, and 1400 cm^{-1}, Figure 8b. They do not reproduce the pairs of bands at 910 and 940 cm^{-1} and 1192 and 1244 cm^{-1}.

The pair of bands at 910 and 940 cm^{-1} are suggestive of the splitting observed for *a*-type, and

– to a lesser extent – *c*-type bands in systems with large rotational constants. We therefore looked for a symmetric $Ta^+CH_2\cdot Ar$ carbene structure, where the Ar is bound to the Ta such that C-Ta-Ar is linear. A $^3B_2$ state of such a species was located and found to have no imaginary frequencies, but it lies relatively high in energy, 1.12 eV above the $^3A''$ ground state. This species has a strong vibration corresponding to the out-of-plane CH_2 wag located at 870 cm^{-1} that corresponds to a *c*-type transition. The rotational band structure shows two equally intense peaks split by 40 cm^{-1} at slightly lower frequencies than those observed. Presumably, this high energy species is kinetically trapped by the cold conditions in the expansion.

With regard to the peaks at 1192 and 1244 cm^{-1}, we were unable to identify a likely source. Ar adducts of the $HTaCH^+$ species in several spin states were considered but none of these has a vibration in the appropriate range. We do note, however, that there is a low-intensity shoulder in the spectrum (both present and literature) for the bare $[Ta,C,2H]^+$ species in a similar frequency range that also has gone unexplained. Presumably, the presence of the Ar narrows the band intensity allowing it to be observed more readily. One possibility for these bands is TaN^+, isobaric with $[Ta,C,2H]^+$. Calculations at the same level of theory used elsewhere indicate this species has a $^2\Sigma$ ground state with a vibrational frequency of 1128 cm^{-1} (no scaling). Ar complexes perpendicular to the TaN^+ bond, leading to a $^2A''$ ground state and a low-lying $^2A'$ state (0.21 eV higher in energy). (In these two complexes, the singly occupied orbital switches between the two 5dδ orbitals of TaN^+.) The TaN^+ vibrations in these two complexes shift to 1097 and 1110 cm^{-1} (no scaling), respectively. These frequencies are too low to reproduce the observed peaks, but it is possible that they are not accurately predicted by the B3LYP approach. Other levels of theory (PBE0, M06, and M06-2X) yield higher frequencies for TaN^+ (1157, 1166, and 1210 cm^{-1}, respectively), with the latter in fair agreement with experiment. For $TaN^+\cdot Ar$, M06-2X predicts frequencies of 1158 ($^2A''$) and 1181 ($^2A'$) cm^{-1}, again somewhat low and with less splitting than observed experimentally.

4. Conclusions

We structurally characterized the products formed by reacting Pt^+ and Ir^+ ions with ethylene oxide (c-C_2H_4O) and Ta^+ with methane under multiple collision conditions using IR spectroscopy. By cooling the reaction channel to 243 K and introducing Ar in the helium carrier gas, a fraction of the $[M,C,2H]^+$ products (M = Ta, Ir, Pt) can be complexed with Ar, allowing for the simultaneous recording of spectra for the bare $[M,C,2H]^+$ ion, via either direct elimination of H for M = Ta and Pt or H_2 for M = Ir, and for its complex with Ar, via loss of Ar.

The spectra for $[Pt,C,2H]^+$ and $[Ir,C,2H]^+$ recorded via direct fragmentation are very similar to those recorded earlier for the products formed upon reacting the metal ions with methane.[19] We therefore conclude that the activation of ethylene oxide results in the same thermodynamically stable $[M,C,2H]^+$ products as the activation of methane. For Pt^+, we find good agreement with the spectrum for the Pt^+CH_2 ($^2A_1$) carbene, whereas for Ir^+ the spectrum is in good agreement with the HIr^+CH ($^1A'$) carbyne-hydride. Under the current conditions, no clear signs of the previously observed Ir^+CH_2 ($^3A_2$) carbene product were found. Consistent with this, we also observe an OIr^+CHCH ($^3A'$) product, for which formation is kinetically favored over that of the carbene. For $[Ta,C,2H]^+$, we reproduce the spectrum obtained previously although the additional cooling reveals obvious structure in one of the bands that can be attributed to the rotational contour.

Spectra of the Ar-complexed $[M,C,2H]^+$ are significantly different from those for the bare product ions, reflecting the non-negligible influence of the Ar atom to both the vibrational frequencies and the rotational constants. Notably, the broad spectral envelopes observed for the bare products are only significantly reduced if the Ar is attached off the principal axis of inertia. The spectra of the Ar complexes are fully consistent with the assignment for the bare complexes. Further, tentative indications for a symmetric Ta^+CH_2 carbene are found when complexed with Ar. The observation of such a species would suggest that electron donation by Ar helps to stabilize the symmetric C_{2v} carbene, which otherwise spontaneously distorts because of the agostic interactions with an empty orbital on Ta. The lower binding energy that needs to be overcome for messenger spectroscopy allows for somewhat better resolved spectral features, which allow us to conclude that significant cooling takes place after expansion into vacuum.

Author Information.

Corresponding Author

*J.M.B.: phone, +31-24-3653952; e-mail, j.bakker@ru.nl

Notes

The authors declare no competing financial interest.

Acknowledgement.

We gratefully acknowledge the Nederlandse Organisatie voor Wetenschappelijk Onderzoek (NWO) for the support of the FELIX Laboratory. This work was supported by the National Science Foundation, Grant No. CHE-1954142. This work was sponsored by NWO Exact and Natural Sciences for the use of supercomputer facilities at SURFsara in Amsterdam (NWO Rekentijd grant 2019.062).

References

(1) Armentrout, P. B. Gas-Phase Perspective on the Thermodynamics and Kinetics of Heterogeneous Catalysis. *Catal. Sci. Technol.* **2014**, *4* (9), 2741.

(2) Roithová, J.; Schröder, D. Selective Activation of Alkanes by Gas-Phase Metal Ions. *Chem. Rev.* **2010**, *110* (2), 1170–1211.

(3) Simon, A.; Lemaire, J.; Boissel, P.; Maître, P. Competition between Agostic WCH_2^+ and $HWCH^+$: A Joint Experimental and Theoretical Study. *J. Chem. Phys.* **2001**, *115* (6), 2510–2518.

(4) Buckner, S. W.; MacMahon, T. J.; Byrd, G. D.; Freiser, B. S. Gas-Phase Reactions of Nb^+ and Ta^+ with Alkanes and Alkenes. C-H Bond Activation and Ligand-Coupling Mechanisms. *Inorg. Chem.* **1989**, *28*, 3511–3518.

(5) Irikura, K. K.; Beauchamp, J. L. Electronic Structure Considerations for Methane Activation by Third-Row Transition Metal Ions. *J. Phys. Chem.* **1991**, *95*, 8344–8351.

(6) Zhang, X.-G.; Liyanage, R.; Armentrout, P. B. Potential Energy Surface for Activation of Methane by Pt^+ : A Combined Guided Ion Beam and DFT Study. *J. Am. Chem. Soc.* **2001**, *123* (23), 5563–5575.

(7) Simon, A.; MacAleese, L.; Boissel, P.; Maître, P. Towards the Characterization of the Mechanism of the Sequential Activation of Four Methane Molecules by Ta^+. *Int. J. Mass Spectrom.* **2002**, *219* (3), 457–473.

(8) Armentrout, P. B.; Shin, S.; Liyanage, R. Guided-Ion Beam and Theoretical Study of the Potential Energy Surface for Activation of Methane by W^+. *J. Phys. Chem. A* **2006**, *110* (4), 1242–1260.

(9) Li, F. X.; Zhang, X. G.; Armentrout, P. B. The Most Reactive Third-Row Transition Metal: Guided Ion Beam and Theoretical Studies of the Activation of Methane by Ir^+. *Int. J. Mass Spectrom.* **2006**, *255*, 279–300.

(10) Parke, L. G.; Hinton, C. S.; Armentrout, P. B. Experimental and Theoretical Studies of the Activation of Methane by Ta^+. *J. Phys. Chem. C* **2007**, *111* (48), 17773–17787.

(11) Parke, L. G.; Hinton, C. S.; Armentrout, P. B. Energetics and Mechanisms of C−H Bond Activation by a Doubly Charged Metal Ion: Guided Ion Beam and Theoretical Studies of $Ta^{2+} + CH_4$. *J. Phys. Chem. A* **2008**, *112* (42), 10469–10480.

(12) Armentrout, P. B.; Parke, L.; Hinton, C.; Citir, M. Activation of Methane by Os^+ : Guided-Ion-Beam and Theoretical Studies. *Chempluschem* **2013**, *78*, 1157–1173.

(13) Fisher, E. R.; Armentrout, P. B. Reactions of Co^+, Ni^+, and Cu^+ with Cyclopropane and Ethylene Oxide. Metal-Methylidene Ion Bond Energies. *J. Phys. Chem.* **1990**, *94* (4), 1674–1683.

(14) Ru, H. G.; Armentrout, P. B.; Chen, Y. Activation of C_2H_6, C_3H_8, $HC(CH_3)_3$, and c-C_3H_6 by Gas-Phase Ru^+ and the Thermochemistry of Ru-Ligand Complexes. *J. Am. Soc. Mass Spectrom.* **1999**, *10*, 821–839.

(15) Aguirre, F.; Husband, J.; Thompson, C. J.; Metz, R. B. Gas-Phase Photodissociation of $AuCH_2^+$: The Dissociation Threshold of Jet-Cooled and Rotationally Thermalized Ions. *Chem. Phys. Lett.* **2000**, *318* (4–5), 466–470.

(16) Armentrout, P. B.; Stevenson, B. C.; Yang, F.; Wensink, F. J.; Lushchikova, O. V.; Bakker, J. M. Infrared Spectroscopy of Gold Carbene Cation ($AuCH_2^+$): Covalent or Dative Bonding? *J. Phys. Chem. A* **2019**, *123* (41), 8932–8941.

(17) Armentrout, P. B. Methane Activation by 5d Transition Metals: Energetics, Mechanisms, and Periodic Trends. *Chem. - A Eur. J.* **2017**, *23* (1), 10–18.

(18) Armentrout, P. B.; Kuijpers, S. E. J.; Lushchikova, O. V; Hightower, R. L.; Boles, G. C.; Bakker, J. M. Spectroscopic Identification of the Carbyne Hydride Structure of the Dehydrogenation Product of Methane Activation by Osmium Cations. *J. Am. Soc. Mass Spectrom.* **2018**, *29* (9), 1781–1790.

(19) Lapoutre, V. J. F.; Redlich, B.; van der Meer, A. F. G.; Oomens, J.; Bakker, J. M.; Sweeney, A.; Mookherjee, A.; Armentrout, P. B. Structures of the Dehydrogenation Products of Methane Activation by 5d Transition Metal Cations. *J. Phys. Chem. A* **2013**, *117* (20), 4115–4126.

(20) Owen, C. J.; Boles, G. C.; Chernyy, V.; Bakker, J. M.; Armentrout, P. B. Structures of the

Dehydrogenation Products of Methane Activation by 5d Transition Metal Cations Revisited: Deuterium Labeling and Rotational Contours. *J. Chem. Phys.* **2018**, *148* (4), 044307.

(21) Markus, C. R.; Thorwirth, S.; Asvany, O.; Schlemmer, S. High-Resolution Double Resonance Action Spectroscopy in Ion Traps: Vibrational and Rotational Fingerprints of $CH_2NH_2^+$. *Phys. Chem. Chem. Phys.* **2019**, *21* (48), 26406–26412.

(22) Asvany, O.; Thorwirth, S.; Redlich, B.; Schlemmer, S. Spectroscopy of the Low-Frequency Vibrational Modes of CH3+ Isotopologues. *J. Mol. Spectrosc.* **2018**, *347*, 1–6.

(23) Lehmann, K. K.; Scoles, G.; Pate, B. H. Intramolecular Dynamics from Eigenstate-Resolved Infrared-Spectra. *Annu. Rev. Phys. Chem.* **1994**, *45*, 241–274.

(24) Beil, A.; Luckhaus, D.; Quack, M.; Stohner, J. Intramolecular Vibrational Redistribution and Unimolecular Reaction: Concepts and New Results on the Femtosecond Dynamics and Statistics in CHBrClF. *Berichte der Bunsen-Gesellschaft* **1997**, *101*, 311–328.

(25) Wheeler, O. W.; Salem, M.; Gao, A.; Bakker, J. M.; Armentrout, P. B. Activation of C–H Bonds in Pt^+ + x CH_4 Reactions, Where x = 1–4: Identification of the Platinum Dimethyl Cation. *J. Phys. Chem. A* **2016**, *120* (31), 6216–6227.

(26) Wheeler, O. W.; Salem, M.; Gao, A.; Bakker, J. M.; Armentrout, P. B. Sequential Activation of Methane by Ir^+: An IRMPD and Theoretical Investigation. *Int. J. Mass Spectrom.* **2019**, *435*, 78–92.

(27) Wheeler, O. W.; Coates, R. A.; Lapoutre, V. J. F.; Bakker, J. M.; Armentrout, P. B. Metallacyclopropene Structures Identified by IRMPD Spectroscopic Investigation of the Dehydrogenation Reactions of Ta^+ and TaO^+ with Ethene. *Int. J. Mass Spectrom.* **2019**, *442* (2019), 83–94.

(28) Okumura, M.; Yeh, L. I.; Lee, Y. T. The Vibrational Predissociation Spectroscopy of Hydrogen Cluster Ions. *J. Chem. Phys.* **1985**, *83* (7), 3705–3706.

(29) Haertelt, M.; Lapoutre, V. J. F.; Bakker, J. M.; Redlich, B.; Harding, D. J.; Fielicke, A.; Meijer, G. Structure Determination of Anionic Metal Clusters via Infrared Resonance Enhanced Multiple Photon Electron Detachment Spectroscopy. *J. Phys. Chem. Lett.* **2011**, *2* (14), 1720–1724.

(30) Bakker, J. M.; Lapoutre, V. J. F.; Redlich, B.; Oomens, J.; Sartakov, B. G.; Fielicke, A.; von Helden, G.; Meijer, G.; van der Meer, A. F. G. Intensity-Resolved IR Multiple Photon Ionization and Fragmentation of C_{60}. *J. Chem. Phys.* **2010**, *132* (7), 074305.

(31) Grimme, S.; Antony, J.; Ehrlich, S.; Krieg, H. A Consistent and Accurate Ab Initio Parametrization of Density Functional Dispersion Correction (DFT-D) for the 94 Elements H-Pu. *J. Chem. Phys.* **2010**, *132* (15), 154104.

(32) Ruscic, B.; Bross, D. H. Active Thermochemical Tables (ATcT) values based on ver. 1.122g of the Thermochemical Network ATcT.anl.gov.

(33) Bakker, J. M.; Besson, T.; Lemaire, J.; Scuderi, D.; Maitre, P. Gas-Phase Structure of a π-Allyl-Palladium Complex: Efficient Infrared Spectroscopy in a 7T Fourier Transform

Mass Spectrometer. *J. Phys. Chem. A* **2007**, *111*, 13415.

(34) Oomens, J.; Sartakov, B. G.; Meijer, G.; von Helden, G. Gas-Phase Infrared Multiple Photon Dissociation Spectroscopy of Mass-Selected Molecular Ions. *Int. J. Mass Spectrom.* **2006**, *254* (1–2), 1–19.

(35) Mehlig, K.; Hansen, K.; Hedén, M.; Lassesson, A.; Bulgakov, A. V; Campbell, E. E. B. Energy Distributions in Multiple Photon Absorption Experiments. *J. Chem. Phys.* **2004**, *120* (9), 4281–4288.

(36) Marks, J. H.; Miliordos, E.; Duncan, M. A. Infrared Spectroscopy of RG–Co^+ (H_2O) Complexes (RG = Ar, Ne, He): The Role of Rare Gas "Tag" Atoms. *J. Chem. Phys.* **2021**, *154* (6), 064306.

Table 1: Frequencies (in cm^{-1}) of observed bands and of the assigned, scaled harmonic vibrations (unshifted values in parentheses) with their mode description.

Species	Observed	Calculated[a]	Mode description	Type
[Pt,C,2H]$^+$	~650	662	CH$_2$ bend, in-plane	*b*
	746	719	Pt-C stretch	*a*
	991	984	CH$_2$ bend, out-of-plane	*c*
[Pt,C,2H]$^+$·Ar	674	681	CH$_2$ bend, in-plane	*b*
	708	681 (720)	CH$_2$ bend, in-plane	*b*
	752	735	Pt-C stretch	*a*
	1050	1031	CH$_2$ bend, out-of-plane	*c*
	1360	1387	CH$_2$ scissor, in-plane	*a*
[Ir,C,2H]$^+$	663	632	H-C-Ir-H bend, in-plane	*b*
	701	690 (747)	CH bend, out-of-plane	*c*
	751[b]	746	OIrCHCH$^+$: CH bend, out-of-plane	*b*
	875[b]	873	OIrCHCH$^+$: CH bend, in-plane	*c*
[Ir,C,2H]$^+$·Ar	673	657	H-C-Ir-H bend, in-plane	*b*
	756	748 (806)	CH bend, out-of-plane	*c*
	1059	1084	Ir-C stretch	*a*
	1360?	1402	CH$_2$ bend, in-plane (carbene)	*a*
[Ir,C,2H]$^+$·Ar$_2$	708	688	H-C-Ir-H bending, in-plane	*b*
	782	747 (805)	CH bending, out-of-plane	*c*
	1068	1088	Ir-C stretch	*a*
[Ta,C,2H]$^+$	700	701	CH$_2$ bend, out-of-plane	*c*
	846	841	Ta-C stretch	*b*
	1334	1304	CH$_2$ bend, in-plane	*b*
[Ta,C,2H]$^+$·Ar	710	712	$^3A''$ CH$_2$ bend, out-of-plane	*c*
	851	841	$^3A''$ Ta-C stretch	*b*
	912	870	$^3B_2$ CH$_2$ bend, out-of-plane	
	939	870		*c*
	1192	1158[c]	$^2A''$ TaN$^+$ stretch	
	1244	1181[c]	$^2A'$ TaN$^+$ stretch	
	1400	1332	$^3A''$ CH$_2$ bend, in-plane	*a*

[a] Scaled by factors detailed in the text. [b] From [Ir,2C,O,2H]$^+$. [c] From TaN$^+$. M06-2X results.

Figure Captions

Fig. 1. IR spectra of $[Pt,C,2H]^+$ (a, top panel, growth in $[Pt,C,H]^+$, black line) and $[Pt,C,2H]^+{\cdot}Ar$ (b, top panel, depletion) accompanied by harmonic fundamental transitions (blue sticks) and rotational envelopes simulated for each transition, calculated for the indicated structures (Pt – blue, C – grey, H – white, Ar – pale blue) at 77 K (black line) and 293 K (red line), in the bottom panel of each graph. Harmonic frequencies were scaled by 0.939 (a) and 0.975 (b), respectively. The red trace in the top panel of b) is a spectrum for $[Pt,C,2H]^+$ formed by reaction of Pt^+ with methane, adapted from Lapoutre *et al.*[19] Dashed vertical lines are guides to the eye.

Fig. 2. Part a) Doublet-spin potential energy surface for $PtCH_2^+$ formation calculated at the B3LYP/def2 level of theory. Part b) Structures associated with the intermediates and TSs in part a. Bond distances between heavy atoms in Å are provided along with relative energies (eV) in parentheses.

Fig. 3. IR spectra of $[Ir,C,2H]^+$ (a, growth spectrum of $[^{191}Ir,C]^+$, black line) and $[Ir,2C,O,2H]^+$ (d, top panel, depletion in red and growth spectrum of $[^{193}Ir,C,2H]^+$ in black). Panels b, c, and e show harmonic fundamental transitions (blue sticks) and rotational envelopes simulated for each transition, calculated for the indicated structures (Ir – blue, C – grey, H – white, O – red) at 77 K (black line). Harmonic frequencies were scaled by 0.95 (b and c) and 0.975 (e), respectively. The red trace in panel a) is a spectrum for $[Ir,C,2H]^+$ formed by reaction of Ir^+ with methane, adapted from Lapoutre *et al.*[19] Dashed vertical lines are guides to the eye.

Fig. 4. IR depletion spectra of $[^{193}Ir,C,2H]^+{\cdot}Ar$ (a, top panel) and $[^{193}Ir,C,2H]^+{\cdot}Ar_2$ (b, top panel) accompanied by harmonic fundamental transitions (blue sticks) and rotational envelopes simulated for each transition, calculated for the indicated structures (Ir – blue, C – grey, H – white, Ar – pale blue) at 77 K (black line) and 293 K (red line). Dashed vertical lines are guides to the eye.***the quality of the embedded structures is not as good as the other figures

Fig. 5. Part a) Potential energy surfaces (quintet – blue, triplet – green, singlet – red) for $HIrCH^+$ and $IrCH_2^+$ formation calculated at the B3LYP/def2 level of theory. Parts b and c) Triplet and singlet structures associated with the intermediates and TSs in part a. Bond distances between heavy atoms in Å are provided along with relative energies (eV) in parentheses.

Fig. 6. Part a) Triplet-spin potential energy surface for $OIrCHCH^+$ formation calculated at the B3LYP/def2 level of theory. The dashed line reproduces the pathway for $IrCH_2^+$ formation in Figure 5a. Part b) Structures associated with the intermediates and TSs in part a. Bond distances between heavy atoms in Å are provided along with relative energies (eV) in parentheses.

Fig. 7. Part a) Potential energy surfaces (triplet – green, singlet – red) for $HIrCH^+$ formation from $OIrCHCH^+$ calculated at the B3LYP/def2 level of theory. Part b) Triplet structures associated with the intermediates and TSs in part a. Bond distances between heavy atoms in Å are provided along with relative energies (eV) in parentheses.

Fig. 8. IR spectra of $[Ta,C,2H]^+$ (a, top panel) and $[Ta,C,2H]^+{\cdot}Ar$ (b, top panel) accompanied by harmonic fundamental transitions (sticks) and simulated rotational envelopes at 77 K (lines) for each transition, calculated for the structures (Ta – blue, C – grey, H – white, Ar – pale blue) indicated, in the bottom panels of each graph. The spectra are color-coded with the states and structures shown. Harmonic frequencies were scaled by 0.98 (a) and 0.975 (b), respectively. The green and red dashed simulated spectra are for the $^2A''$ and $^2A'$ structures of $TaN^+{\cdot}Ar$ (M06-2X/def2 results), multiplied by a factor of 10. The red trace in panel a) is a spectrum for $[Ta,C,2H]^+$ formed by reaction of Ta^+ with methane, adapted from Lapoutre *et al.*[19]

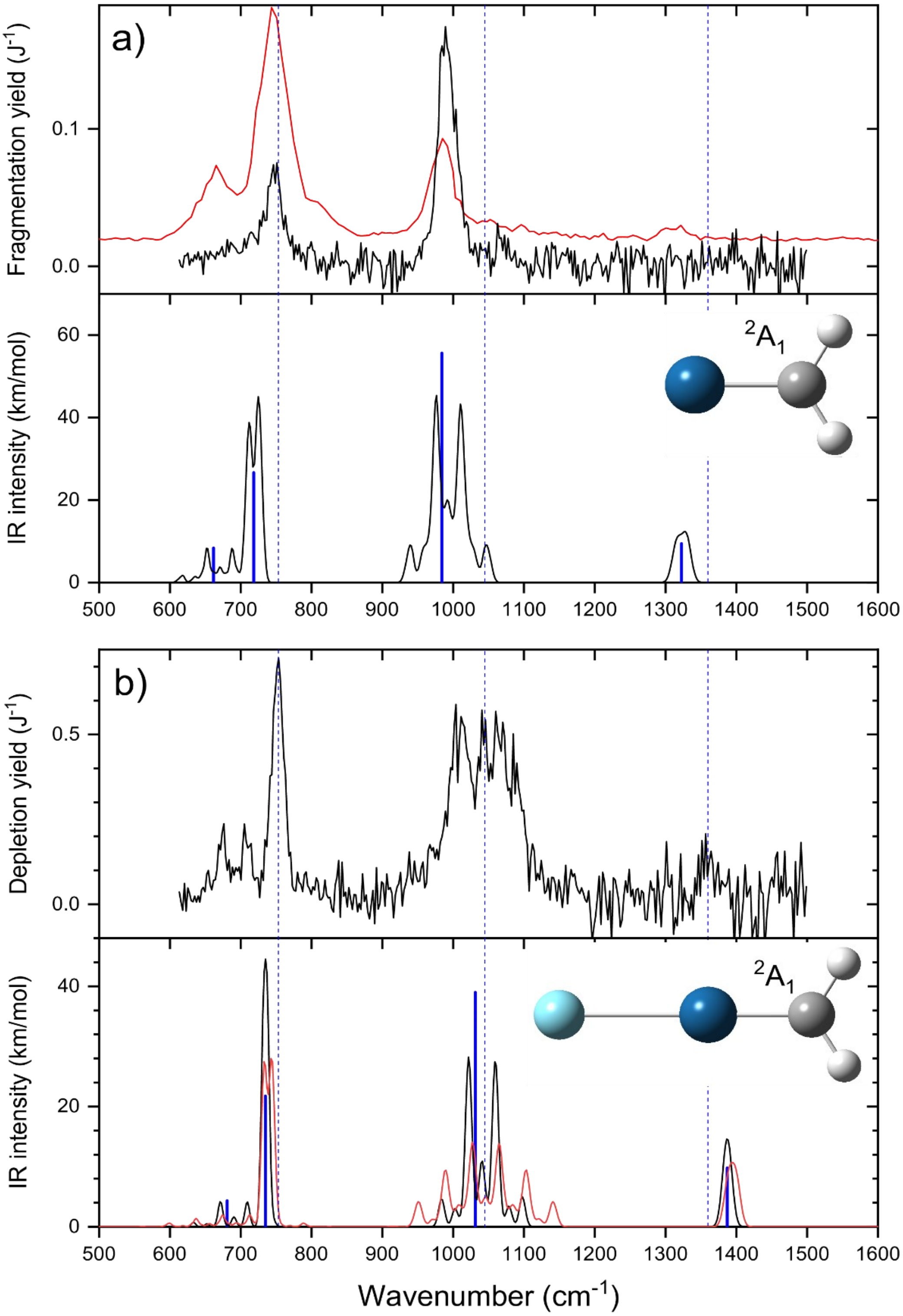
a)
Fragmentation yield (J-1)
0.1
0.0
IR intensity (km/mol)
60
40
20
0
2A1
500
600
700
800
900
1000
1100
1200
1300
1400
1500
1600
b)
Depletion yield (J-1)
0.5
0.0
IR intensity (km/mol)
40
20
0
2A1
Wavenumber (cm-1)

Figure 1

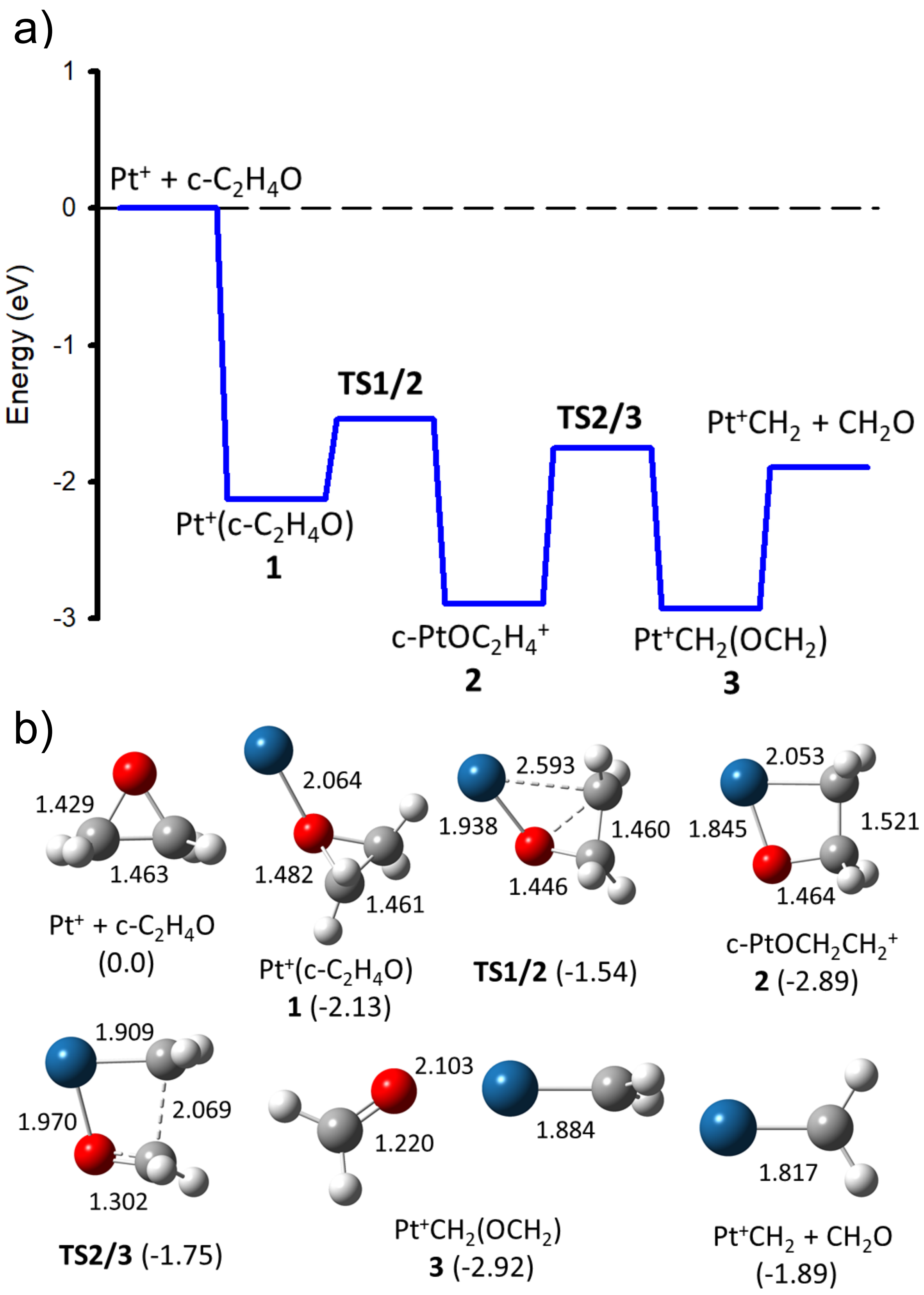
a)
Energy (eV)
1
0
-1
-2
-3
Pt⁺ + c-C₂H₄O
Pt⁺(c-C₂H₄O)
1
TS1/2
c-PtOC₂H₄⁺
2
TS2/3
Pt⁺CH₂(OCH₂)
3
Pt⁺CH₂ + CH₂O
b)
1.429
1.463
Pt⁺ + c-C₂H₄O
(0.0)
2.064
1.482
1.461
Pt⁺(c-C₂H₄O)
1 (-2.13)
2.593
1.938
1.460
1.446
TS1/2 (-1.54)
2.053
1.845
1.521
1.464
c-PtOCH₂CH₂⁺
2 (-2.89)
1.909
1.970
2.069
1.302
TS2/3 (-1.75)
2.103
1.220
1.884
Pt⁺CH₂(OCH₂)
3 (-2.92)
1.817
Pt⁺CH₂ + CH₂O
(-1.89)

Figure 2

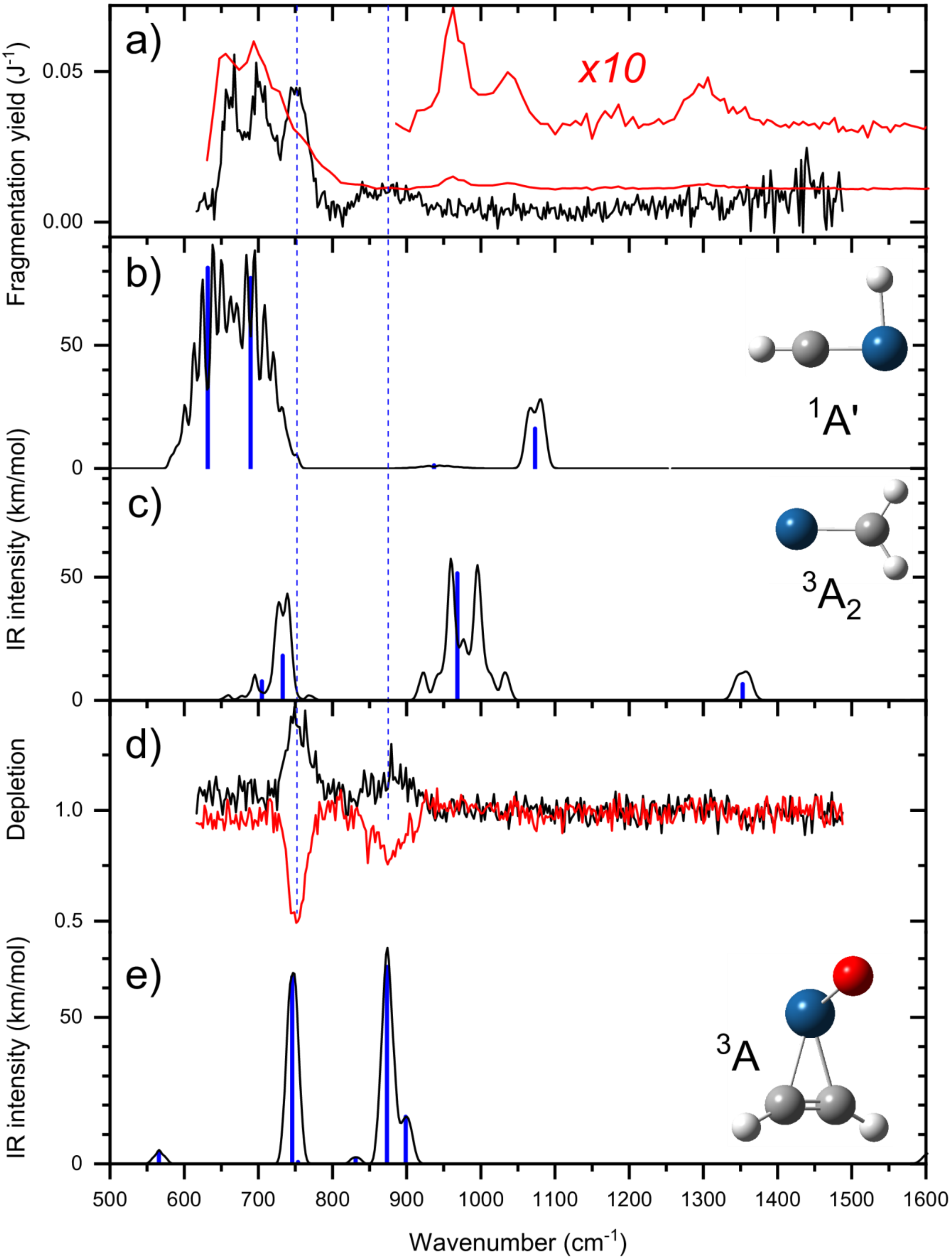
a)
x10
Fragmentation yield (J^{-1})
0.05
0.00
b)
$^1A'$
50
0
c)
$^3A_2$
IR intensity (km/mol)
50
0
d)
Depletion
1.0
0.5
e)
^3A
IR intensity (km/mol)
50
0
500
600
700
800
900
1000
1100
1200
1300
1400
1500
1600
Wavenumber (cm^{-1})

Figure 3

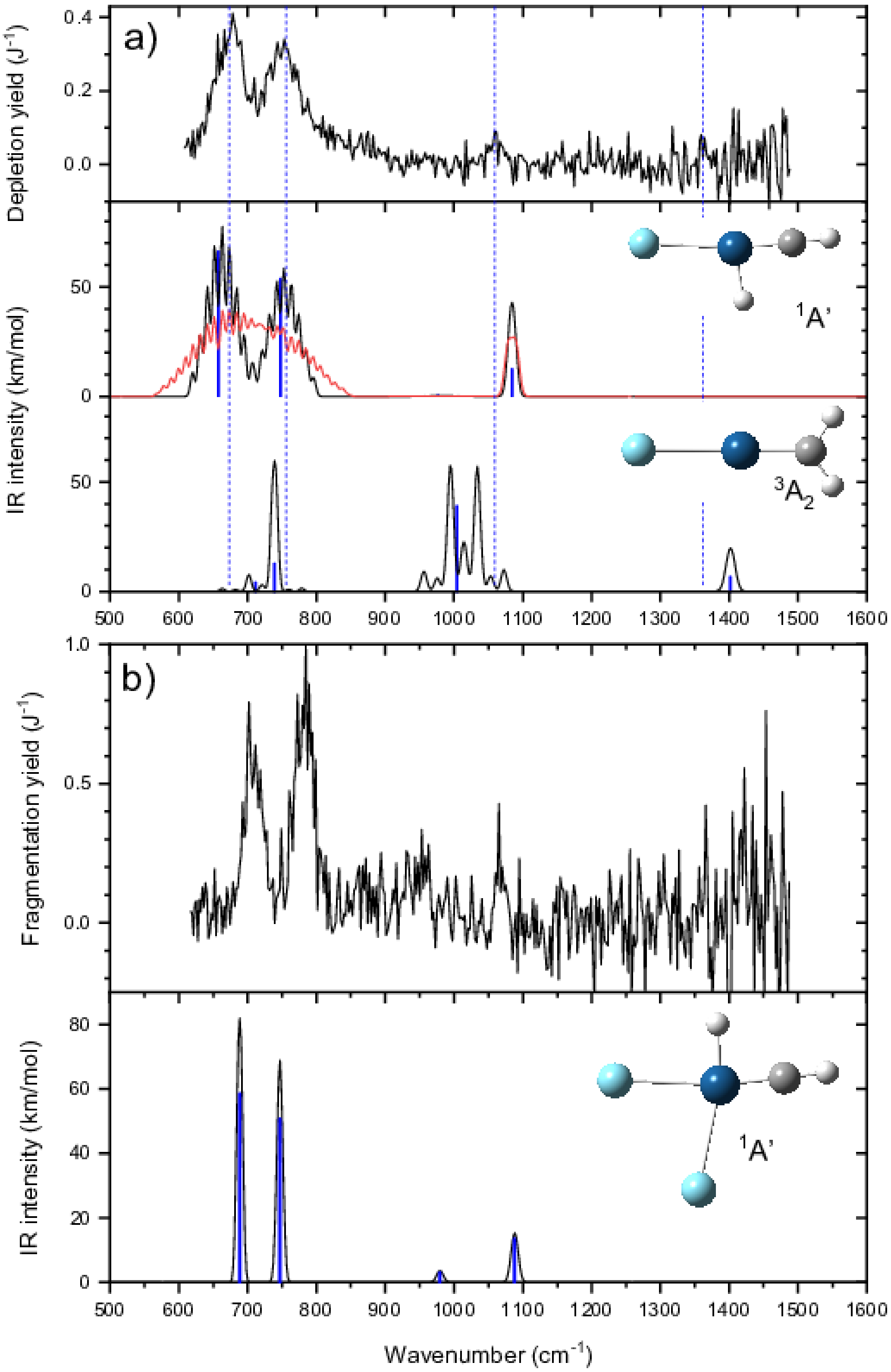
a)
b)
Depletion yield (J^{-1})
IR intensity (km/mol)
Fragmentation yield (J^{-1})
IR intensity (km/mol)
^{1}A'
^{3}A$_2$
^{1}A'
Wavenumber (cm^{-1})
0.4
0.2
0.0
50
0
50
0
1.0
0.5
0.0
80
60
40
20
0
500
600
700
800
900
1000
1100
1200
1300
1400
1500
1600

Figure 4

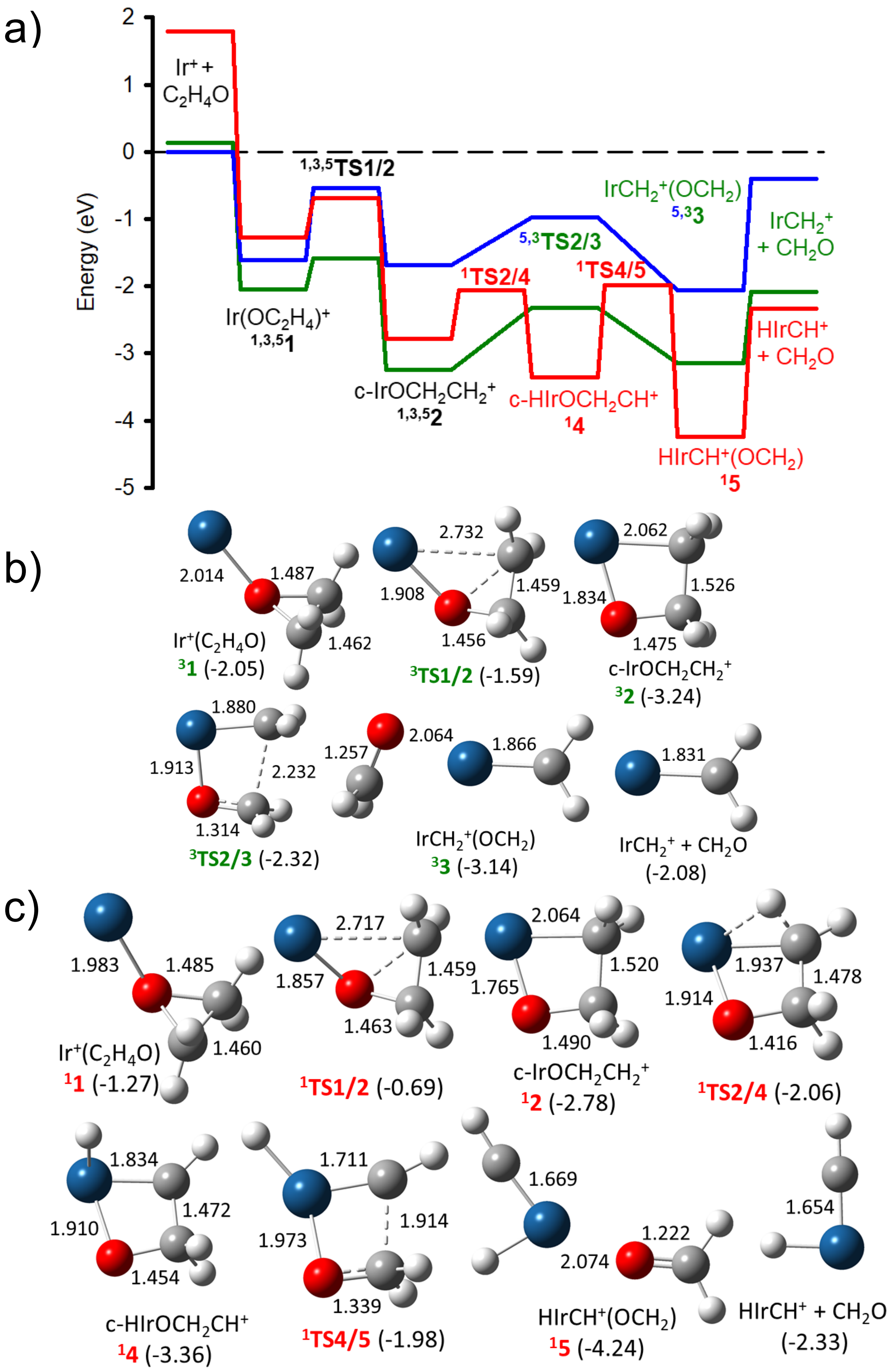
a)
Energy (eV)
2
1
0
-1
-2
-3
-4
-5
$Ir^+ + C_2H_4O$
^{1,3,5}TS1/2
$IrCH_2^+(OCH_2)$
^{5,3}3
$IrCH_2^+ + CH_2O$
^{5,3}TS2/3
^{1}TS2/4
^{1}TS4/5
$Ir(OC_2H_4)^+$
^{1,3,5}1
$HIrCH^+ + CH_2O$
c-$IrOCH_2CH_2^+$
^{1,3,5}2
c-$HIrOCH_2CH^+$
^{1}4
$HIrCH^+(OCH_2)$
^{1}5
b)
2.014
1.487
1.462
$Ir^+(C_2H_4O)$
^{3}1 (-2.05)
2.732
1.908
1.459
1.456
^{3}TS1/2 (-1.59)
2.062
1.834
1.526
1.475
c-$IrOCH_2CH_2^+$
^{3}2 (-3.24)
1.880
1.913
2.232
1.314
^{3}TS2/3 (-2.32)
1.257
2.064
1.866
$IrCH_2^+(OCH_2)$
^{3}3 (-3.14)
1.831
$IrCH_2^+ + CH_2O$
(-2.08)
c)
1.983
1.485
1.460
$Ir^+(C_2H_4O)$
^{1}1 (-1.27)
2.717
1.857
1.459
1.463
^{1}TS1/2 (-0.69)
2.064
1.765
1.520
1.490
c-$IrOCH_2CH_2^+$
^{1}2 (-2.78)
1.937
1.914
1.478
1.416
^{1}TS2/4 (-2.06)
1.834
1.910
1.472
1.454
c-$HIrOCH_2CH^+$
^{1}4 (-3.36)
1.711
1.973
1.914
1.339
^{1}TS4/5 (-1.98)
1.669
2.074
1.222
$HIrCH^+(OCH_2)$
^{1}5 (-4.24)
1.654
$HIrCH^+ + CH_2O$
(-2.33)

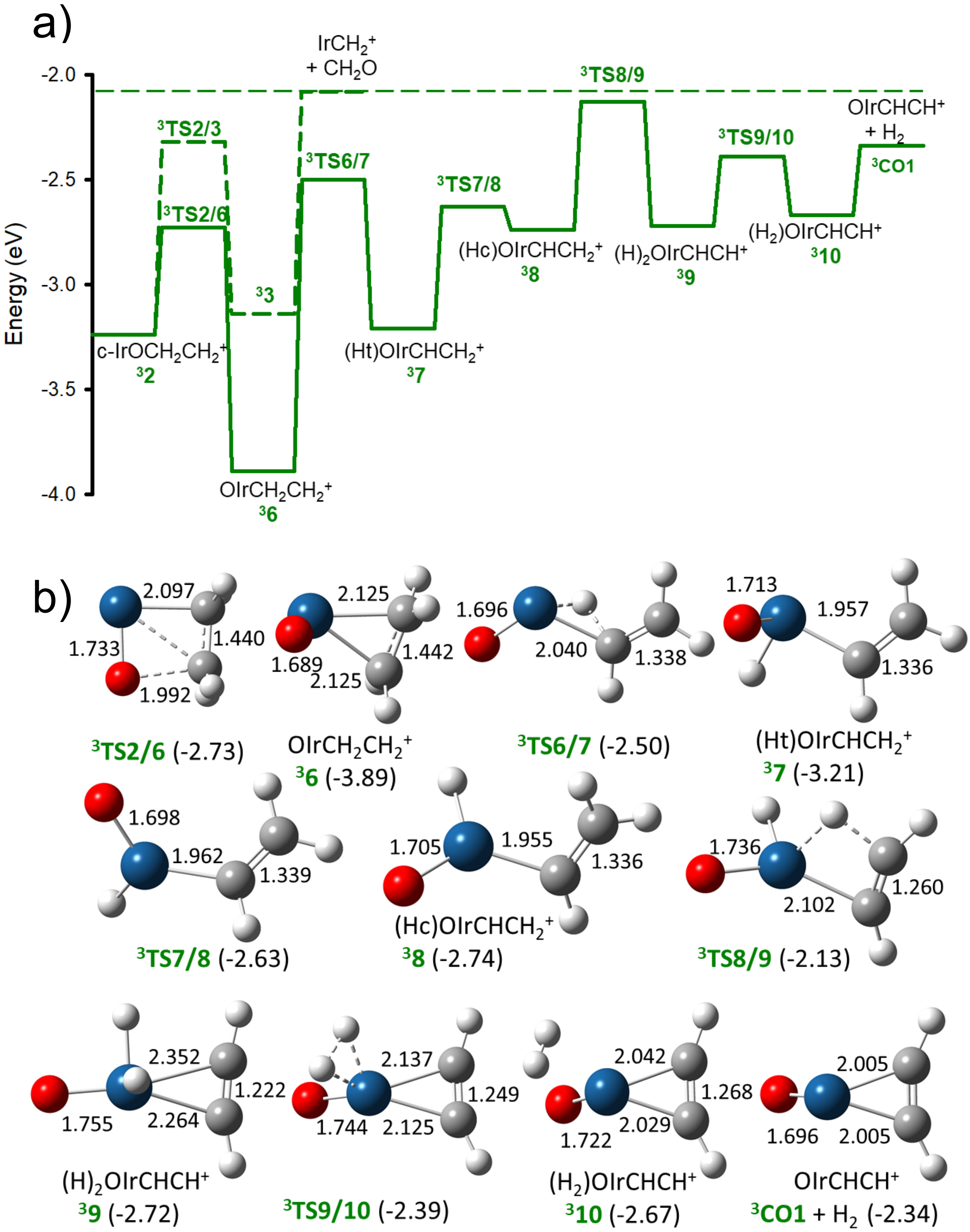
a)
-2.0
-2.5
-3.0
-3.5
-4.0
Energy (eV)
IrCH2+ + CH2O
3TS2/3
3TS2/6
33
c-IrOCH2CH2+
32
OIrCH2CH2+
36
3TS6/7
(Ht)OIrCHCH2+
37
3TS7/8
(Hc)OIrCHCH2+
38
3TS8/9
(H)2OIrCHCH+
39
3TS9/10
(H2)OIrCHCH+
310
OIrCHCH+ + H2
3CO1
b)
2.097
1.733
1.440
1.992
3TS2/6 (-2.73)
2.125
1.689
2.125
1.442
OIrCH2CH2+
36 (-3.89)
1.696
2.040
1.338
3TS6/7 (-2.50)
1.713
1.957
1.336
(Ht)OIrCHCH2+
37 (-3.21)
1.698
1.962
1.339
3TS7/8 (-2.63)
1.705
1.955
1.336
(Hc)OIrCHCH2+
38 (-2.74)
1.736
2.102
1.260
3TS8/9 (-2.13)
2.352
1.222
1.755
2.264
(H)2OIrCHCH+
39 (-2.72)
2.137
1.249
1.744
2.125
3TS9/10 (-2.39)
2.042
1.268
1.722
2.029
(H2)OIrCHCH+
310 (-2.67)
2.005
1.696
2.005
OIrCHCH+
3CO1 + H2 (-2.34)

Figure 6

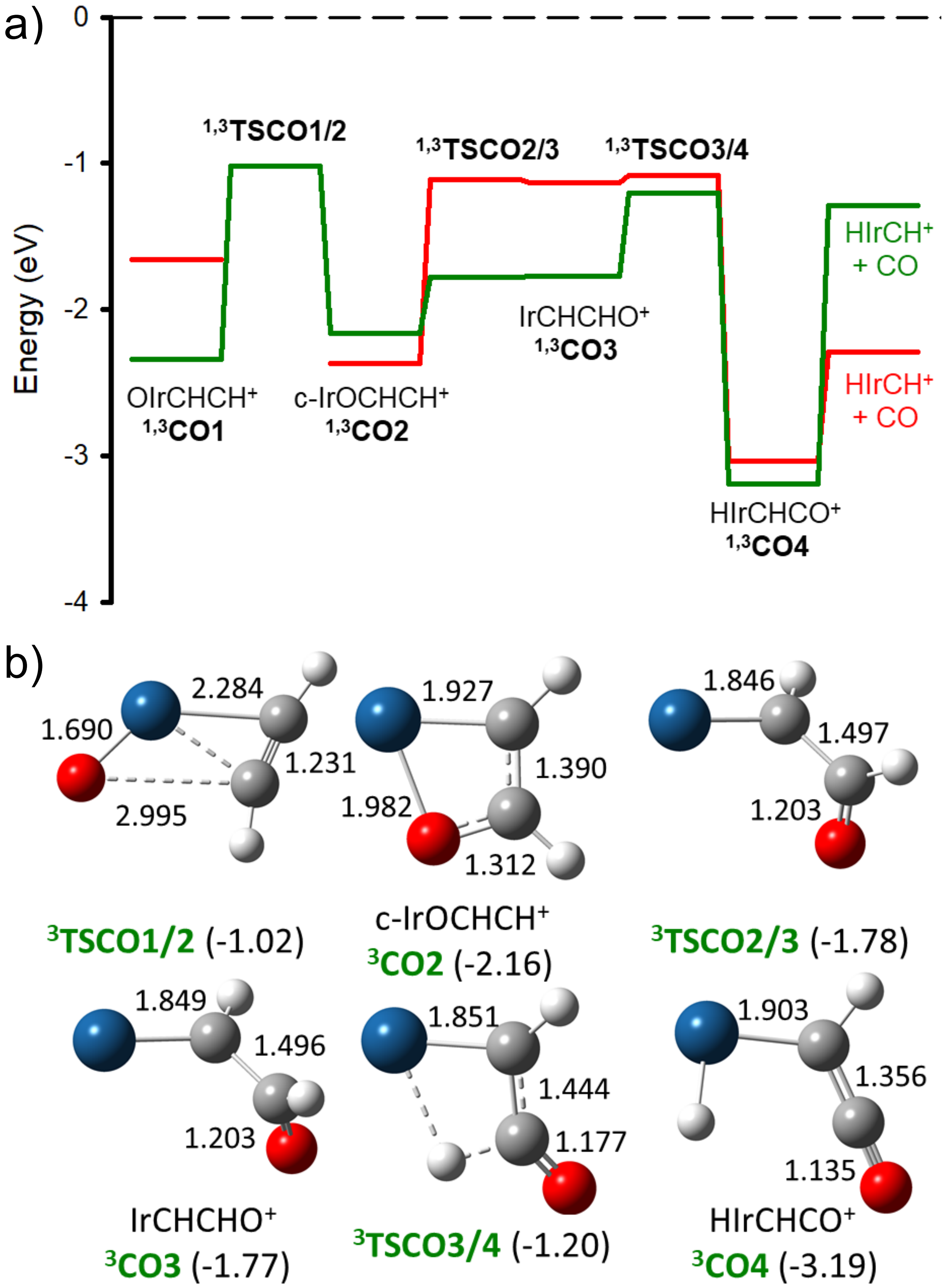
a)
0
-1
-2
-3
-4
Energy (eV)
1,3TSCO1/2
1,3TSCO2/3
1,3TSCO3/4
HIrCH+ + CO
IrCHCHO+ 1,3CO3
OIrCHCH+ 1,3CO1
c-IrOCHCH+ 1,3CO2
HIrCH+ + CO
HIrCHCO+ 1,3CO4
b)
2.284
1.690
1.231
2.995
1.927
1.390
1.982
1.312
1.846
1.497
1.203
3TSCO1/2 (-1.02)
c-IrOCHCH+
3CO2 (-2.16)
3TSCO2/3 (-1.78)
1.849
1.496
1.203
1.851
1.444
1.177
1.903
1.356
1.135
IrCHCHO+
3CO3 (-1.77)
3TSCO3/4 (-1.20)
HIrCHCO+
3CO4 (-3.19)

Figure 7

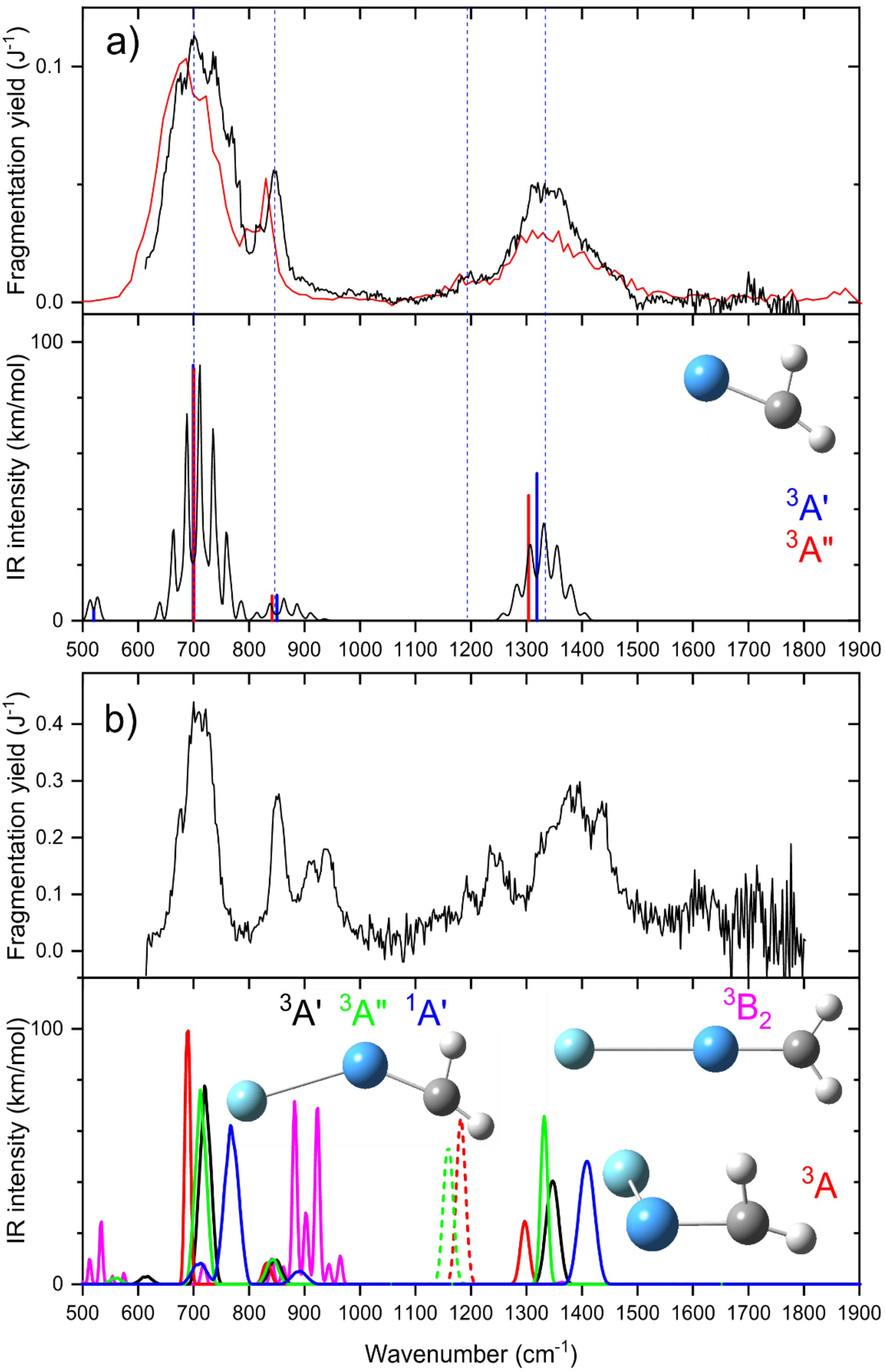
a)
Fragmentation yield (J^{-1})
0.1
0.0
IR intensity (km/mol)
100
0
^{3}A'
^{3}A"
500
600
700
800
900
1000
1100
1200
1300
1400
1500
1600
1700
1800
1900
b)
Fragmentation yield (J^{-1})
0.4
0.3
0.2
0.1
0.0
IR intensity (km/mol)
100
0
^{3}A'
^{3}A"
^{1}A'
^{3}B$_2$
^{3}A
Wavenumber (cm^{-1})

Figure 8

SUPPORTING INFORMATION

Table S1: Rotational constants (in cm^{-1}) of observed species calculated at the B3LYP-D3/def2-TZVPPD level of theory.

Species	State	A	B	C
$[Pt,C,2H]^+$	$^2A_1$	9.4815	0.3537	0.3410
$[Pt,C,2H]^+\cdot Ar$	$^2A_1$	9.6687	0.0553	0.0550
$[Ir,C,2H]^+$	$^1A'$	6.9506	0.4438	0.4172
	$^3A_2$	9.6239	0.3478	0.3356
$[Ir,C,2H]^+\cdot Ar$	$^1A'$	5.5027	0.0580	0.0574
	$^3A_2$	9.8208	0.0528	0.0525
$[Ir,C,2H]^+\cdot Ar_2$	$^1A'$	0.0669	0.0552	0.0302
$[Ta,C,2H]^+$	$^3A'$	12.3638	0.3489	0.3394
	$^3A''$	12.0773	0.3465	0.3368
$[Ta,C,2H]^+\cdot Ar$	$^3A'$	1.0913	0.0546	0.0520
	$^3A''$	1.0552	0.0543	0.0516
	$^1A'$	1.7907	0.0533	0.0518
	^3A	0.3607	0.0656	0.0560
	$^3B_2$	10.2082	0.0405	0.0403
$[Ta,N]^+\cdot Ar$	$^2A'$	0.5120	0.0708	0.0622
	$^3A''$	0.5073	0.0743	0.0648

Figure Captions

Fig. S1. Schematic of the source, interaction of molecular beam with IR laser, and mass spectrometric detection of the ions. Not shown are the slit aperture shaping the molecular beam, and the slit aperture in the time-of-flight mass spectrometer.

Fig. S2. Mass spectrum of the product distribution resulting from reaction of Pt$^+$ with ethylene oxide in an argon-seeded helium carrier gas.

Fig. S3. Mass spectrum of the product distribution resulting from reaction of Ir$^+$ with ethylene oxide in an argon-seeded helium carrier gas.

Fig. S4. Mass spectrum of the product distribution resulting from reaction of Ta$^+$ with methane in an argon-seeded helium carrier gas.

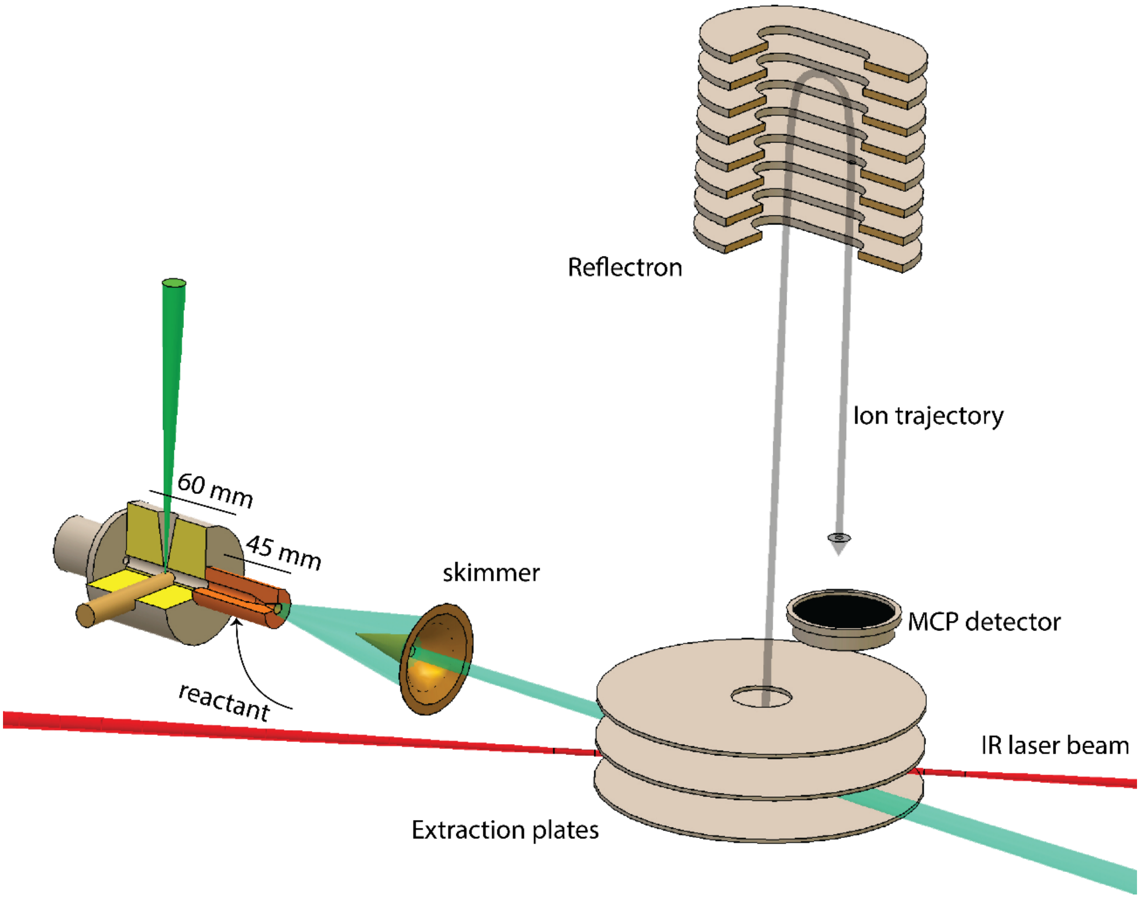
Reflectron
Ion trajectory
60 mm
45 mm
skimmer
MCP detector
reactant
IR laser beam
Extraction plates

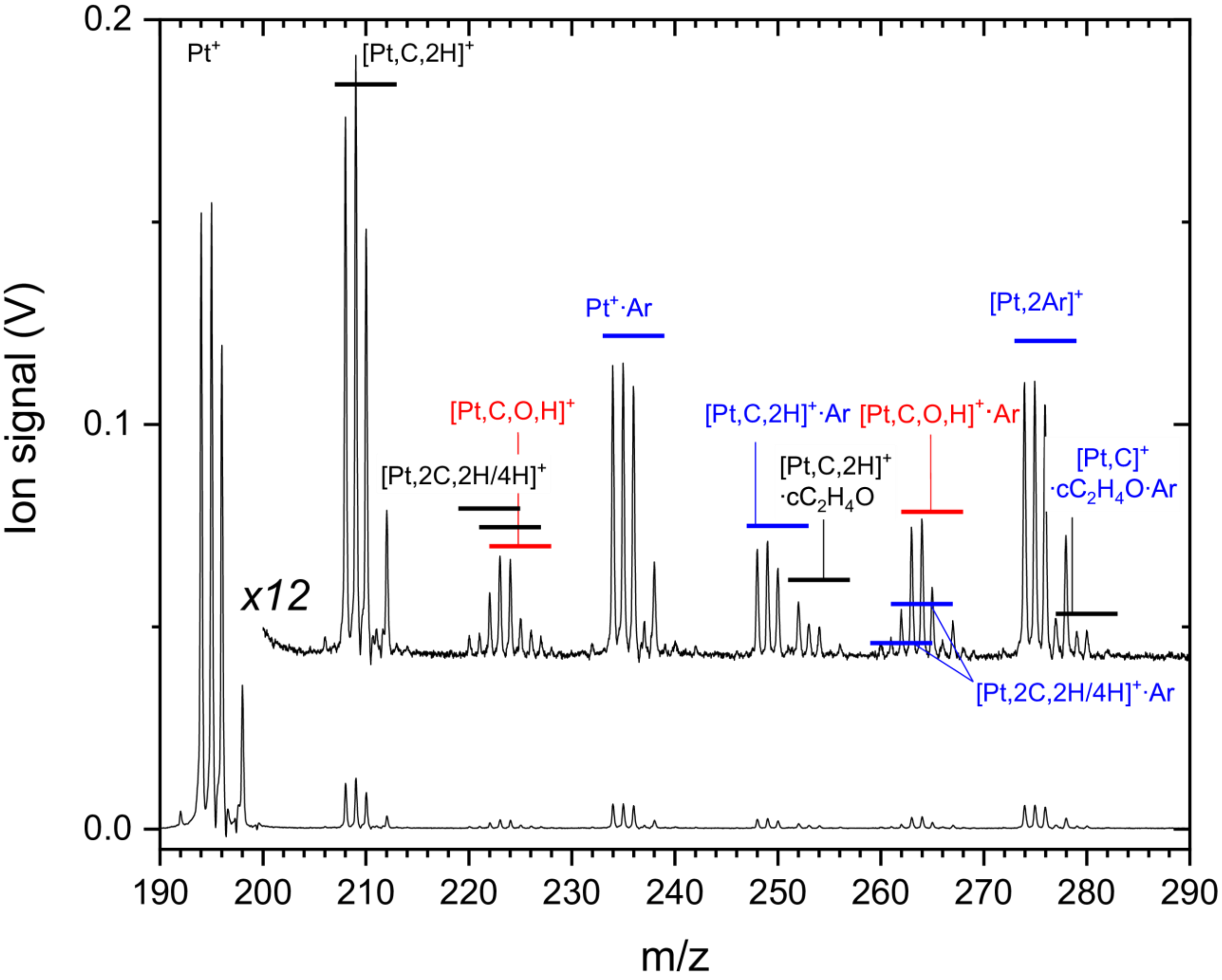
Pt⁺
[Pt,C,2H]⁺
x12
[Pt,C,O,H]⁺
[Pt,2C,2H/4H]⁺
Pt⁺·Ar
[Pt,C,2H]⁺·Ar
[Pt,C,2H]⁺ ·cC₂H₄O
[Pt,C,O,H]⁺·Ar
[Pt,2Ar]⁺
[Pt,C]⁺ ·cC₂H₄O·Ar
[Pt,2C,2H/4H]⁺·Ar
Ion signal (V)
0.0
0.1
0.2
m/z
190
200
210
220
230
240
250
260
270
280
290

Figure S2

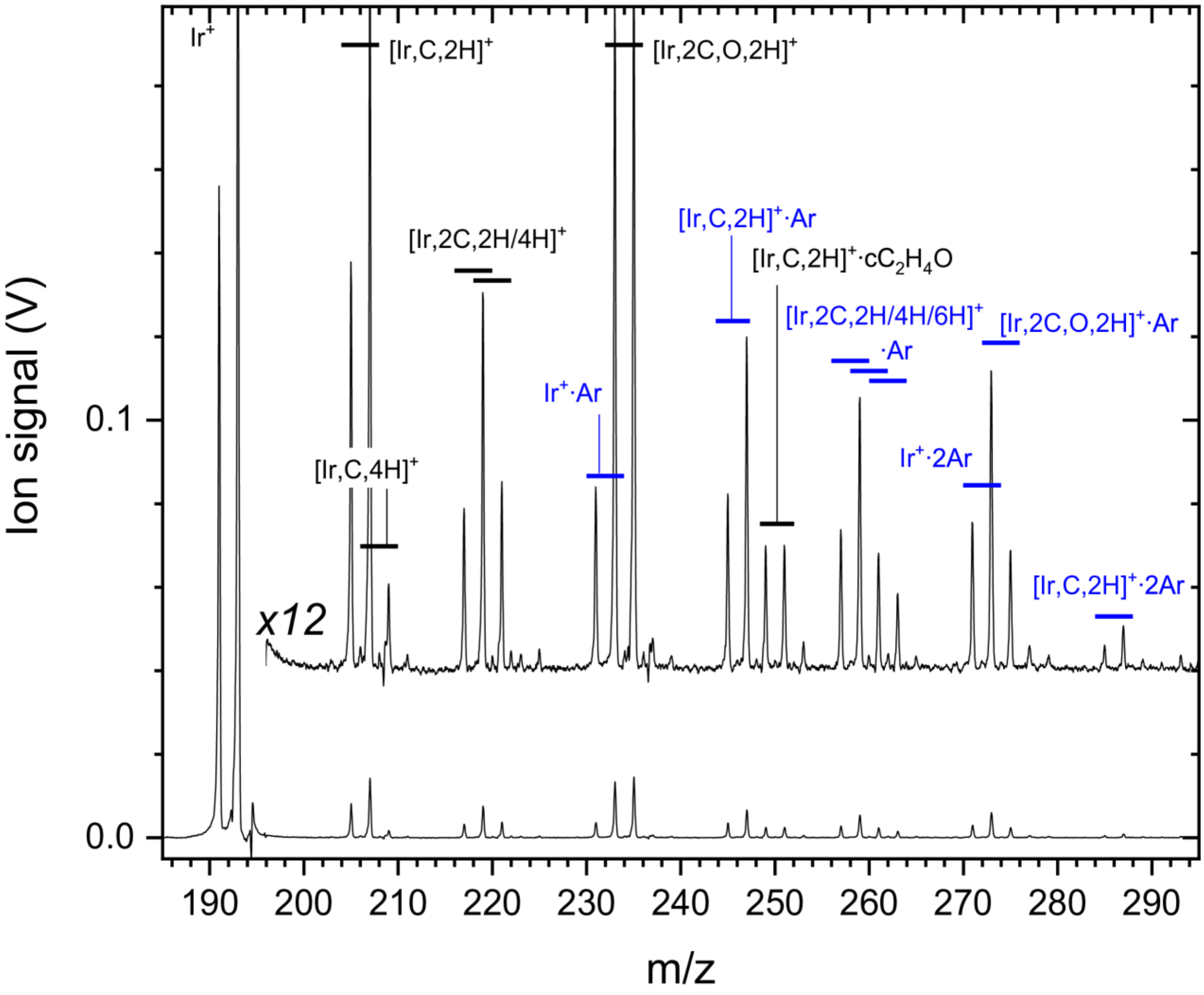
Ir^+
$[Ir,C,2H]^+$
$[Ir,2C,O,2H]^+$
$[Ir,2C,2H/4H]^+$
$[Ir,C,2H]^+\cdot Ar$
$[Ir,C,2H]^+\cdot cC_2H_4O$
$[Ir,2C,2H/4H/6H]^+ \cdot Ar$
$[Ir,2C,O,2H]^+\cdot Ar$
$Ir^+\cdot Ar$
$[Ir,C,4H]^+$
$Ir^+\cdot 2Ar$
$[Ir,C,2H]^+\cdot 2Ar$
x12
Ion signal (V)
0.1
0.0
190
200
210
220
230
240
250
260
270
280
290
m/z

Figure S3

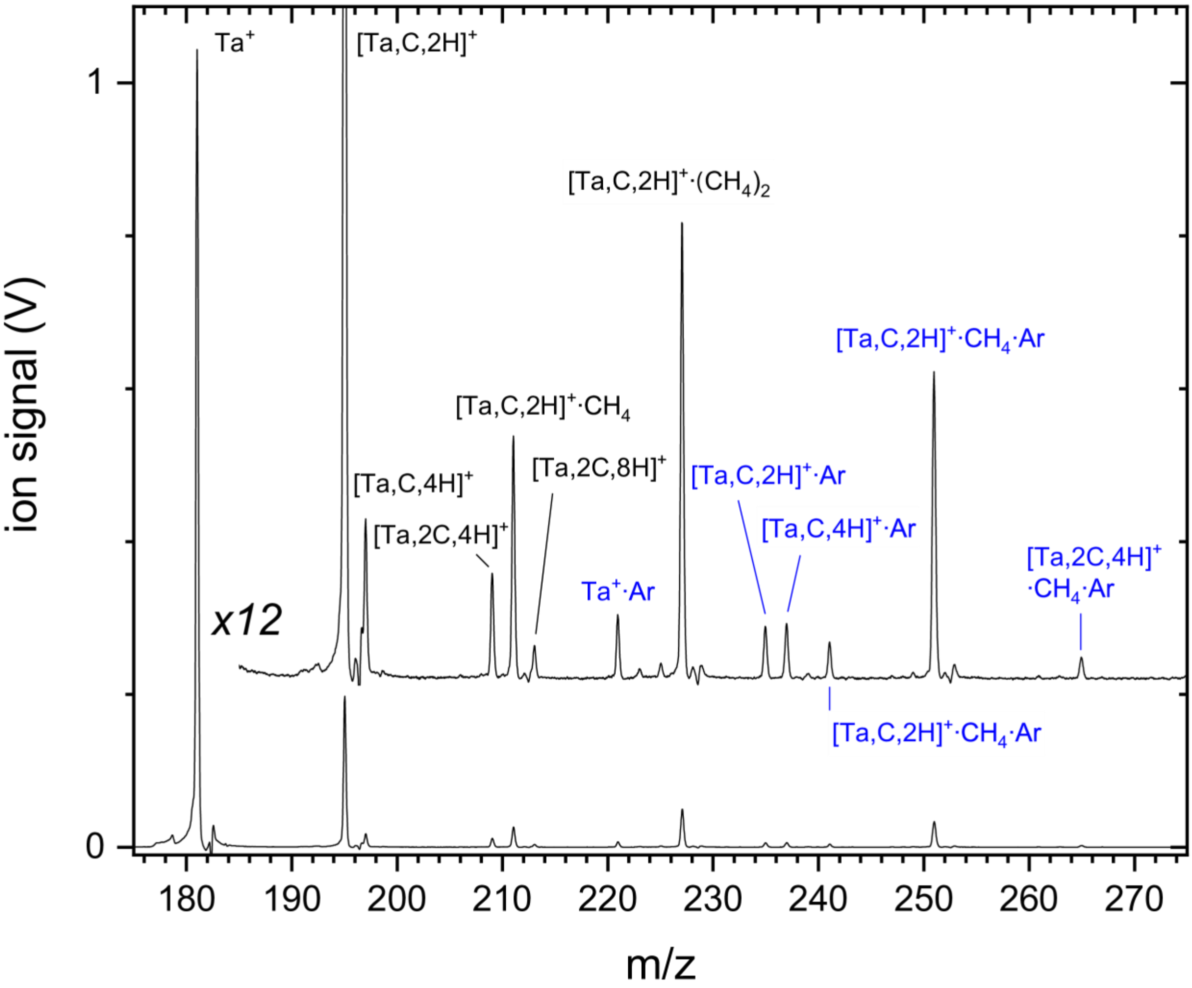
ion signal (V)
m/z
1
0
180
190
200
210
220
230
240
250
260
270
x12
Ta$^+$
[Ta,C,2H]$^+$
[Ta,C,2H]$^+$·(CH$_4$)$_2$
[Ta,C,2H]$^+$·CH$_4$
[Ta,C,4H]$^+$
[Ta,2C,4H]$^+$
[Ta,2C,8H]$^+$
Ta$^+$·Ar
[Ta,C,2H]$^+$·Ar
[Ta,C,4H]$^+$·Ar
[Ta,C,2H]$^+$·CH$_4$·Ar
[Ta,2C,4H]$^+$
·CH$_4$·Ar
[Ta,C,2H]$^+$·CH$_4$·Ar

Figure S4